

NAT'L INST. OF STAND & TECH



A11106 229107

NBS

PUBLICATIONS

NBSIR 81-1647

# LASER-INITIATED COMBUSTION STUDIES OF SELECTED ALUMINUM, COPPER, IRON, AND NICKEL ALLOYS

---

James W. Bransford

Alan F. Clark

Thermophysical Properties Division  
National Engineering Laboratory  
National Bureau of Standards  
Boulder, Colorado 80303

April 1981

QC

100

.U56

81-1647

1981

c.2



NBSIR 81-1647

NATIONAL BUREAU  
OF STANDARDS  
LIBRARY  
JUL 20 1981

170-200-1132  
Acme  
1132  
NO. 81-1647  
1981  
2.07

# LASER-INITIATED COMBUSTION STUDIES OF SELECTED ALUMINUM, COPPER, IRON, AND NICKEL ALLOYS

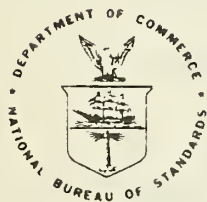
---

James W. Bransford

Alan F. Clark

Thermophysical Properties Division  
National Engineering Laboratory  
National Bureau of Standards  
Boulder, Colorado 80303

April 1981



---

U.S. DEPARTMENT OF COMMERCE, Malcolm Baldrige, Secretary

NATIONAL BUREAU OF STANDARDS, Ernest Ambler, Director



## CONTENTS

	Page
LIST OF TABLES . . . . .	v
LIST OF FIGURES . . . . .	vi
ABSTRACT . . . . .	viii
I. INTRODUCTION . . . . .	1
II. EXPERIMENTAL . . . . .	6
III. RESULTS . . . . .	11
A. Aluminum Alloys 1100, 2219, 6061, and Tensile-50 . . . . .	11
B. Stainless Ferrous Alloys 304, 347, and 21-6-9 . . . . .	31
C. Nickel Alloy Inconel 600 . . . . .	42
D. Copper Alloys . . . . .	46
1. Beryllium-Copper . . . . .	46
2. Bronze . . . . .	47
IV. CONCLUSIONS AND RECOMMENDATIONS . . . . .	55
A. Conclusions . . . . .	55
1. Aluminum Alloys . . . . .	55
a. Ignition . . . . .	55
b. Combustion . . . . .	56
2. Stainless Ferrous Alloys and Nickel Alloys . . . . .	56
a. Ignition . . . . .	56
b. Combustion . . . . .	57
3. Copper Alloys . . . . .	57
a. Ignition . . . . .	57
b. Combustion . . . . .	58
4. Areas of Uncertainty . . . . .	58

B. Recommendations . . . . .	59
V. ACKNOWLEDGMENTS . . . . .	60
Appendix A. Temperature Measurement Using the Thermal Radiation	
Spectrum . . . . .	61
Appendix B. Two-Color Pyrometer Theory . . . . .	64
by Key Nguyen and M. C. Branch	
I. INTRODUCTION . . . . .	64
II. THEORY OF THE MEASUREMENT METHOD . . . . .	65
III. DETERMINATION OF THE SPECTRAL EMISSIVITY RATIO . . . . .	68
IV. DESCRIPTION OF THE APPARATUS . . . . .	71
A. Two-Color Pyrometer . . . . .	71
B. Spectral Emissivity Ratio Measuring Device . . . . .	73
V. THE VALIDITY OF THE THERMAL EQUILIBRIUM ASSUMPTION . . . . .	78

LIST OF TABLES

	PAGE
Table 1. FACTORS AFFECTING METAL IGNITION AND COMBUSTION. . . . .	4
Table 2. MAJOR COMPONENTS OF ALLOYS STUDIED . . . . .	5
Table 3. COMBUSTION TEMPERATURES. . . . .	16
Table B-1. SPECIFICATIONS OF ARGON ION LASER . . . . .	76
Table B-2. POWER OUTPUT OF THE ARGON ION LASER. . . . .	77

## LIST OF FIGURES

	PAGE
Figure 1. Experimental setup. . . . .	7
Figure 2. General instrument hook-up. . . . .	8
Figure 3a. Continuum spectra for Aluminum Alloy 1100. 400 to 800 nm wavelength range. . . . .	13
Figure 3b. Bandhead spectra for Aluminum Alloy 1100. . . . .	13
Figure 4. Graph of thermal emission spectrum for temperature determination . . . . .	14
Figure 5. Graph of thermal emission spectrum for temperature determination . . . . .	15
Figure 6. Vapor pressure of Al and Al <sub>2</sub> O <sub>3</sub> . . . . .	17
Figure 7. 1100 Aluminum Alloy combustion rate and radiant intensity . .	19
Figure 8. Fraction of 1100 Aluminum Alloy remaining during combustion .	20
Figure 9. Log fraction remaining for 1100 Aluminum Alloy. . . . .	21
Figure 10. 2219 Aluminum Alloy combustion rate and radiant intensity . .	22
Figure 11. Fraction of 2219 Aluminum Alloy remaining during combustion .	23
Figure 12. Log fraction remaining for 2219 Aluminum Alloy. . . . .	24
Figure 13. 6061 Aluminum Alloy combustion rate and radiant intensity . .	25
Figure 14. Fraction of 6061 Aluminum Alloy remaining during combustion .	26
Figure 15. Log fraction remaining for 6061 Aluminum Alloy. . . . .	27
Figure 16. Tensile-50 Aluminum Alloy combustion rate and radiant intensity . . . . .	28
Figure 17. Fraction of Tensile-50 Aluminum Alloy remaining during combustion. . . . .	29
Figure 18. Log fraction remaining for Tensile-50 Aluminum Alloy. . . . .	30
Figure 19. 304 Stainless Steel combustion rate and radiant intensity . .	33
Figure 20. Fraction of 304 Stainless Steel remaining during combustion .	34
Figure 21. Log fraction remaining for 304 Stainless Steel. . . . .	35
Figure 22. 347 Stainless Steel combustion rate and radiant intensity . .	36

Figure 23.	Fraction of 347 Stainless Steel remaining during combustion . . .	37
Figure 24.	Log fraction remaining for 347 Stainless Steel. . . . .	38
Figure 25.	21-6-9 Stainless Steel combustion rate and radiant intensity. . .	39
Figure 26.	Fraction of 21-6-9 Stainless Steel remaining during combustion. . . . .	40
Figure 27.	Log fraction remaining for 21-6-9 Stainless Steel . . . . .	41
Figure 28.	Inconel 600 combustion rate and radiant intensity . . . . .	43
Figure 29.	Fraction of Inconel 600 remaining during combustion . . . . .	44
Figure 30.	Log fraction remaining for Inconel 600. . . . .	45
Figure 31.	Beryllium-Copper combustion rate and radiant intensity. . . . .	48
Figure 32.	Fraction of Beryllium-Copper alloy remaining during combustion. . . . .	49
Figure 33.	Log fraction remaining for Beryllium-Copper alloy . . . . .	50
Figure 34.	Bronze combustion rate and radiant intensity. . . . .	52
Figure 35.	Fraction of Bronze alloy remaining during combustion. . . . .	53
Figure 36.	Log fraction remaining for Bronze alloy . . . . .	54
Figure B1.	Schematic of temperature measurement system . . . . .	72
Figure B2.	Chopper disk. . . . .	74
Figure B3.	Alternator disk . . . . .	74
Figure B4.	Characteristic conduction times of Al-1100, Ni and Inconel 600 . . . . .	80

LASER-INITIATED COMBUSTION STUDIES OF SELECTED  
ALUMINUM, COPPER, IRON, AND NICKEL ALLOYS\*

James W. Bransford and Alan F. Clark  
National Bureau of Standards  
Boulder, Colorado 80303

The results of combustion studies at atmospheric pressure on ten metal alloys are presented. The alloys studied were aluminum alloys 1100, 2219, 6061, and tensile-50; 304, 347 and 21-6-9 stainless steel; inconel 600; beryllium-copper and a bronze. It was found that once ignition was achieved all alloys would generally burn to completion. The overall combustion process appears to obey a first-order rate process. Preliminary conclusions are presented along with recommendations for future work.

Key words: alloys; combustion; combustion rate; ignition; metals; oxygen atmosphere; temperature measurement.

\*Certain commercial equipment, instruments, and materials are identified in this paper to adequately specify the experimental procedure and materials studied. In no case does such identification imply recommendation or endorsement by the National Bureau of Standards, nor does it imply that the material or equipment identified is necessarily the best available for the purpose.

## I. INTRODUCTION

The advent of large scale use of liquid and gaseous oxygen by the defense establishments in the late nineteen forties and early nineteen fifties resulted in the clear recognition that serious materials compatibility problems existed. These problems were centered around organic compounds used for seals, lubricants and other components, and around the metallic alloys of aluminum, magnesium and titanium. In order to select the most oxygen-compatible materials, an impact test method and apparatus was developed at the Army Ballistic Missile Agency during the mid nineteen fifties. This method was, in general, adequate for selecting materials used in rocket and ground support systems at that time and later for the early manned space program. However, as higher stress levels were reached in various rocket and ground support system components - from increased pressure, flow velocities, component operating speeds, etc. - it was recognized that the original test apparatus and methods were probably inadequate. Thus, several new test methods and apparatus were developed to extend the pressure and temperature range and to utilize other ignition techniques. However, the impact tester, modified to operate at high pressure, is still the primary device used to evaluate materials for oxygen service. Several versions of the high-pressure oxygen impact tester have been used to evaluate space shuttle engine materials.

As the testing of the space shuttle main engine materials progressed it was found that all metallic materials passed the applicable impact test except the aluminum alloys. These aluminum alloys fracture readily upon impact whereas the other high strength engine metallic materials do not. As

individual component and engine testing commenced, facility and components began to fail through metal ignition and combustion. Several of the failures were very extensive and costly. With these failures it became readily apparent that detailed knowledge of the metal ignition and combustion processes was seriously lacking. Consequently this study of the metal ignition and combustion processes was begun by the National Bureau of Standards sponsored by NASA's George C. Marshall Space Flight Center.

In initiating a study on metal ignition and combustion, several major aspects to the problem should be understood at the beginning. These are:

1. At room temperature, the reaction



is spontaneous, to the right, for every metal element except gold. For the metal elements that are used to form high strength alloys this spontaneity to the right continues for at least one oxide, and usually more, to very high temperatures. Thus the tendency to oxidize at high rates (burn) is strong.

2. The metal-oxygen reaction is heterogeneous involving gas, liquid, and solid phases. The reaction products are usually refractory and thus complicate the description and study of the chemical process due to latent heats, and melting and boiling points.
3. High pressure complicates the experimental procedure used to study metal combustion. Equipment that can ordinarily be used in the open

must be adapted for use in pressure chambers and shielded from heat and splatter, or alternative means of study must be found. Examples of this are the need to adapt an electronic balance for high pressure use or the potential involvement of the containment vessel itself.

4. A large number of parameters are involved in the ignition and combustion process. Many of these parameters are temperature dependent, and this dependency is only poorly known, if known at all. Table 1 contains an extensive list of such parameters.

The initial effort has been to apply methods previously utilized in the study of titanium combustion to metals and alloys of interest to space applications. A listing of the materials studied is shown in Table 2. The methods employed to date are high speed cinematography, emission spectra, combustion intensity, combustion temperature, and mass uptake. Schlieren and Hilbert transform methods will be employed later to determine flame distribution.

In general, it was found that all alloys, except bronze, were somewhat difficult to ignite, especially inconel and beryllium-copper. This difficulty was caused by the reflectivity of the specimen and by the oxide layer formed during the heat-up period. However, once ignited, the alloys generally burned with vigor and essentially to completion. The manner of combustion varied from the "skating sun" of the aluminum alloys to a very active type with ejection of material by the steel alloys and inconel to the quiet combustion of the bronze.

The following sections will discuss in turn the experimental setup, results, conclusions and recommendations resulting from the work to date.

TABLE 1: FACTORS AFFECTING METAL IGNITION AND COMBUSTION

Material Properties*	Environmental	Configuration
<p>atomic weight (m)                      molecular weight (mo)                      thermal conductivity (m+mo)                      thermal diffusivity (m+mo)                      heat capacity (m+mo)                      heats of solid phase transitions (m+mo)                      heat of fusion (m+mo)                      heat of vaporization (m+mo)                      heat of formation (m+mo)                      melting point (m+mo)                      boiling point (m+mo)                      ignition temperature (m)                      vapor pressure (m+mo)                      viscosity (m+mo)                      surface tension (m+mo)                      solubility of oxygen in metal (m)                      diffusivity of oxygen (m+mo)                      diffusivity of metal (m+mo)                      emissivity (m+mo)                      composition of metal (m)                      chemical reaction rates (m+mo)                      equilibrium constants (mo)                      solubility of oxygen in reaction products                      solubility of metal in reaction products                      density (m+mo)                      thermal expansion (m+mo)                      convective heat transfer coefficients</p>	<p>temperature                      pressure                      oxygen concentration                      presence of diluent                      nature of diluent                      gas velocity                      Reynolds number</p>	<p>history of metal                      state of surface                      oxide film thickness                      specific surface area (cm<sup>2</sup>/g)                      total mass of metal                      presence of other metals                      (eutectic formation or                      thermite reaction possible)                      presence of contaminants                      centrifugal forces                      angle of attack                      heat and mass transfer                      coefficients</p>

\*m = metal

mo = metal oxide

TABLE 2: MAJOR COMPONENTS OF ALLOYS STUDIED

% Composition

	Aluminum Alloys				Ferrous Alloys			Nickel Alloy	Copper Alloys	
	1100	2219	6061	Tens. -50	304	347	21-6-9	Inconel 600	2% Be	Bronze
Al	98.7	92.8	96.2	91.3						
Be									1.9	
Cr					19	18	20	16		
Cu	0.2	6.3	0.28					0.1	98	89.9
Fe	1.0	0.3	0.7		68	70	63	7		
Mg			1.0	0.5						
Mn		0.3	0.2		2		9.5	0.2		
Nb						1				
Ni					10	11	7	76		0.4
Si		0.2	0.6	8.0	1		0.15	0.2		
Sn										8
Zn	0.1	0.1	0.3							1.4

## II. EXPERIMENTAL

The initial experiments have been carried out in the open using the arrangement of Figure 1. Ten alloys were studied. These were the aluminum alloys 1100, 2219, 6061, and Tensile-50; 304, 347 and 21-6-9 stainless steels; inconel 600; bronze and beryllium-copper. The 40 to 300 mg specimens were blanketed with flowing oxygen and irradiated with a focused 100 W CW CO<sub>2</sub> laser beam. Since the alloys studied are generally difficult to ignite at ambient pressure conditions, the specimens were insulated from the high thermal conductivity graphite support block with a thin granular layer of aluminum oxide or asbestos material. These two materials have high melting points and do not oxidize; therefore, it is believed they will not change the ignition or combustion characteristics of the alloys. Even with this insulating layer most materials, notably inconel and beryllium-copper, were still difficult to ignite. A large part of this difficulty can be explained by the high reflectivity and emissivity of the alloys and alloy oxides and the high temperature that must be achieved for ignition. These temperatures are generally the melting point of aluminum oxide for the aluminum alloys and the alloy melting point for the other materials. Typical heating times before ignitions varied from about 15 seconds to more than a minute.

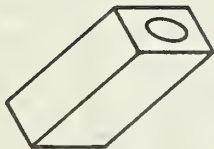
The general experimental arrangement is shown schematically in Figure 2. The photodiode used in this study is a silicon PIN photovoltaic device with a spectral response that peaks at approximately 850 nm. This type of response curve makes the diode a good device for detecting the beginning of the thermal runaway oxidation of the alloys studied. Thus, the amplified photodiode signal

**Carbon Dioxide**

**Laser**



**Rapid Scan  
Spectrometer**



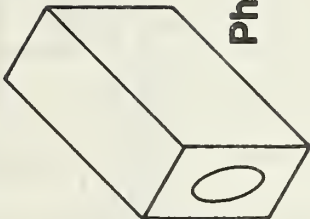
**Object Lens**



**Free Flowing  
Oxygen**



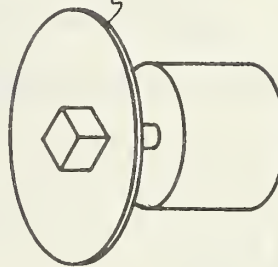
**Photodiode**



**High Speed  
Movie Camera**



**Graphite  
Support**



**Mass  
Scale**

Figure 1. Experimental setup.

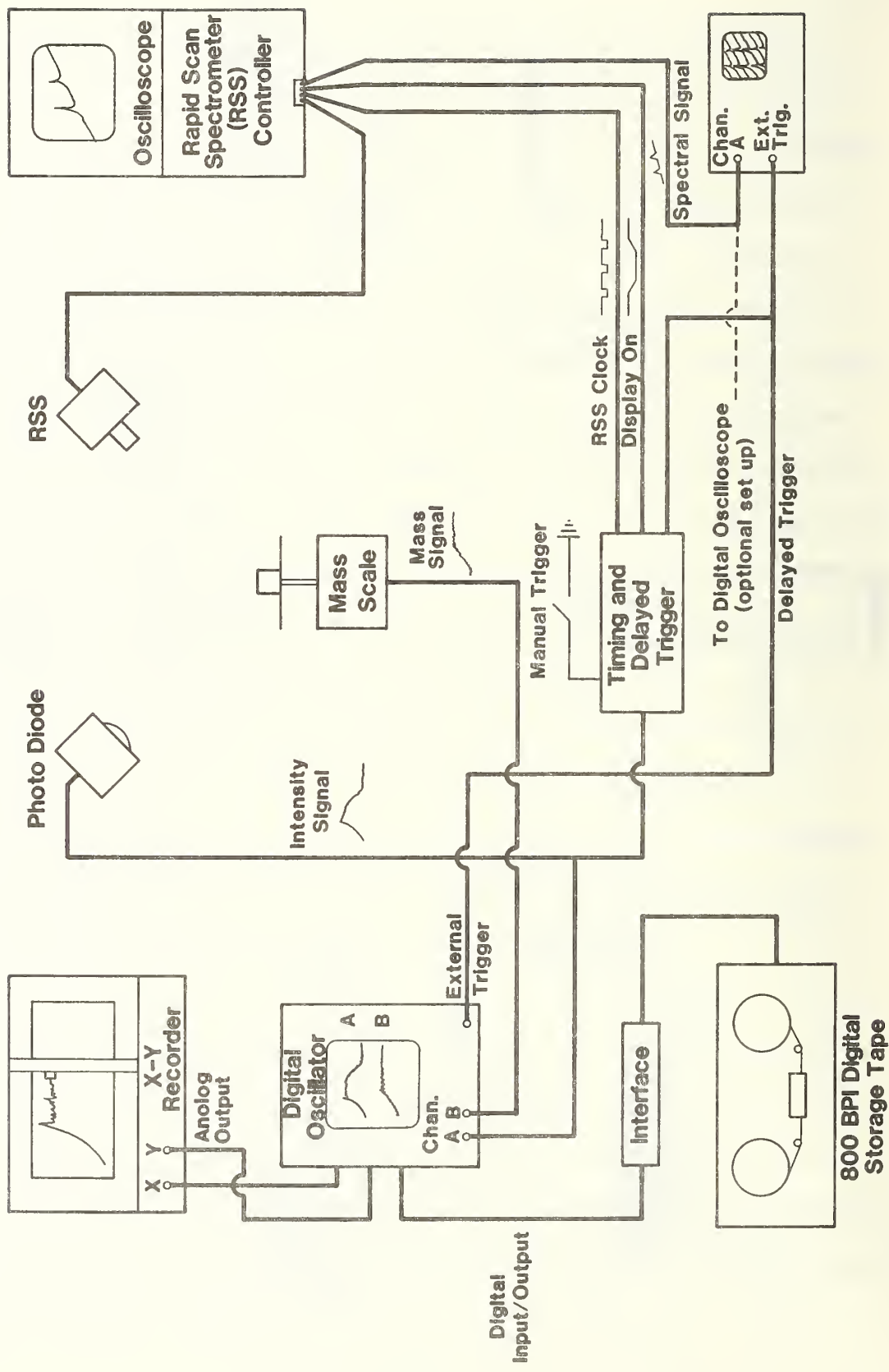


Figure 2. General instrument hook-up.

can be used as a trigger source for other instrumentation as well as a monitor of the relative radiant intensity of the burning sample.

Spectra were obtained using a Tektronix J20/7J20 rapid scanning spectrometer (RSS). This unit, which has two diffraction gratings, has a first order spectral response range from 300 nm to 1100 nm. The spectrum can be scanned in intervals as large as 400 nm or as small as 4 nm. The region to be studied is focused, by an external lens, onto the entrance slit of the J20 unit. The light passing through the slit is diffracted by a grating onto the surface of a vidicon tube constructed of charge-storage diodes. An electron beam scans the vidicon and ultimately an analog signal representing time-resolved spectral power (incident optical power versus wavelength) is produced. This signal can then be recorded photographically from an oscilloscope or digitally by a digital oscilloscope. Spectra thus obtained were used to identify reacting vapor species or to determine combustion temperatures.

Combustion rates can be estimated from the mass increase of the burning specimen. To obtain this mass increase an electronic balance, modified to increase its response time, was used. Since the combustion process usually had a very violent period with the ejection of particles, a thin glass hood with openings for the laser beam and oxygen, was placed over the specimen. Even with this hood a small amount of material was lost because of vapor and particles ejected through the holes by the specimen during its most active combustion period. The particle ejection was also detected by the balance and the resulting spikes in the mass signal partially obscures some portions of the mass-gain curve. The balance was also slightly sensitive to heat transmitted

through the pan assembly to the suspension. This heat sensitivity was generally noticeable only for the aluminum alloys which required longer heating times before ignition and also have a higher heat of combustion than the other alloys. The maximum mass loss was approximately 20 percent for one aluminum alloy sample to only a few percent for a bronze. The deviation from stoichiometric weight for each alloy is noted on each mass increase graph as the ratio  $W_i/W_s$ . Where  $W_i$  is the initial weight of the alloy sample and  $W_s$  is the total weight of the oxidation products.

The behavior of the alloys before and after ignition was determined by high-speed cinematography. Framing rates were approximately 300 fps. A high-speed tungsten balanced (3200 K) color film was used.

Combustion temperatures were measured by using the Rapid Scanning Spectrometer. The development of the procedure by which the combustion temperature is determined from a radiant intensity vs. wavelength scan is given in Appendix A. Since the electronic recording equipment used was only capable of recording a total of four scans, multiple scans at fixed time intervals were recorded on a single film. From these scans one was selected that represented the highest combustion radiant intensity. The radiant intensity was then determined at selected wavelengths. Those data was then used with a linear least squares procedure to determine the combustion temperature at the time of highest radiant intensity.

### III. RESULTS

As stated previously five types of measurements were made on each alloy studied. The results of these measurements will be discussed below for each alloy or alloy system.

#### A. Aluminum Alloys 1100, 2219, 6061 and Tensile-50

The four aluminum alloys had essentially the same ignition and combustion characteristics. This similarity can be seen in the combustion mass increase and radiant intensity traces in Figures 7, 10, 13, and 16 and in the high speed movies. The combustion sequence, for these alloys, can be broken into two separate stages; the induction or heat-up stage and the combustion stage.

During the induction stage, the sample develops a tight thick oxide layer. This layer has sufficient strength to maintain the original sample shape after the sample temperature has increased beyond the alloy melting point. Ignition appears to occur when the oxide melts or fractures near the oxide melting point from internal pressure and/or thermal stresses and exposes the molten alloy to the oxygen atmosphere. The ignition spot is usually small but spreads rapidly over the sample melting the oxide layer and converting the sample into a molten drop. The beginning of the combustion stage is marked by a vigorous combustion usually accompanied by the ejection of small molten drops of material. Since the molten oxides produced by the combustion, predominately  $Al_2O_3$ , are not miscible with the molten alloys, two phases soon separate with the lower density alloy floating on the oxides. This phase separation continues with the molten

alloy "skating" on the oxide surface until combustion is complete. A great deal of smoke is generated during the combustion stage along with a fine spray and some larger droplets of the molten alloy. The spray droplets generally are ejected with a momentum too low to be picked up distinctly by the electronic balance; however, the larger droplets can be detected and are seen as sharp spikes in the mass electrical signal.

Spectra of the combustion region show strong vibrational band heads in the emission spectra from 440 nm to 560 nm wavelength as shown in Figure 3a; an expanded bandhead is shown in Figure 3b. These band heads have been attributed to the gaseous AlO molecule [Zhdanova and Sokolov]. The AlO molecule is primarily produced in the Al vapor - O<sub>2</sub> gaseous reaction zone above the surface of the liquid alloy sample and is subsequently oxidized to Al<sub>2</sub>O<sub>3</sub>.

In spite of the band heads, sufficient continuum exists so that a combustion temperature can be determined. Figure 3a shows a typical oscilloscope photograph that was used for this purpose and Figures 4 and 5 show typical graphs of data obtained from several photographs. Table 3 summarizes the results for a number of these measurements. The temperature values given are for the maximum stable combustion temperature. This value is usually reached within several tenth's of a second after ignition and then slowly decreases until combustion is complete. Occasionally flare temperatures, generally at the start of combustion, appear to have higher temperatures. However, these last for too short a time to be measured by the present instrumentation. The temperature of the molten sample should be approximately 2300 K (see Figure 6), the approximate boiling point at our altitude of the aluminum alloys

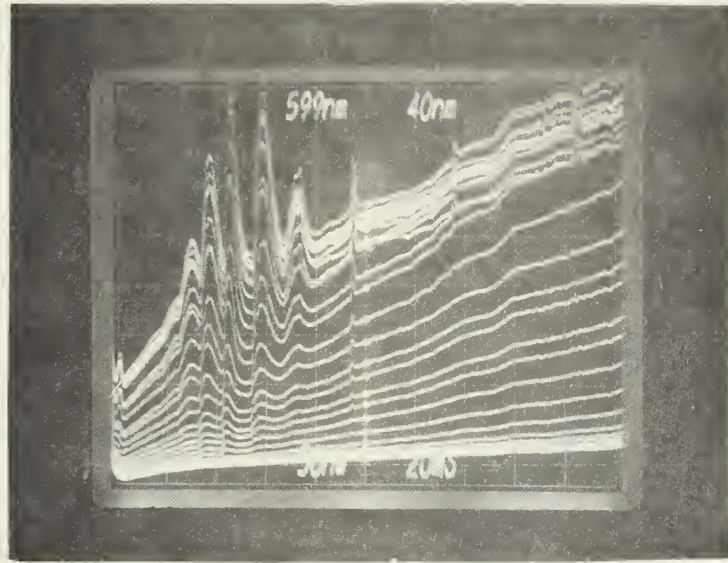


Figure 3a. Continuum spectra for Aluminum Alloy 1100. 400 to 800 nm wavelength range.

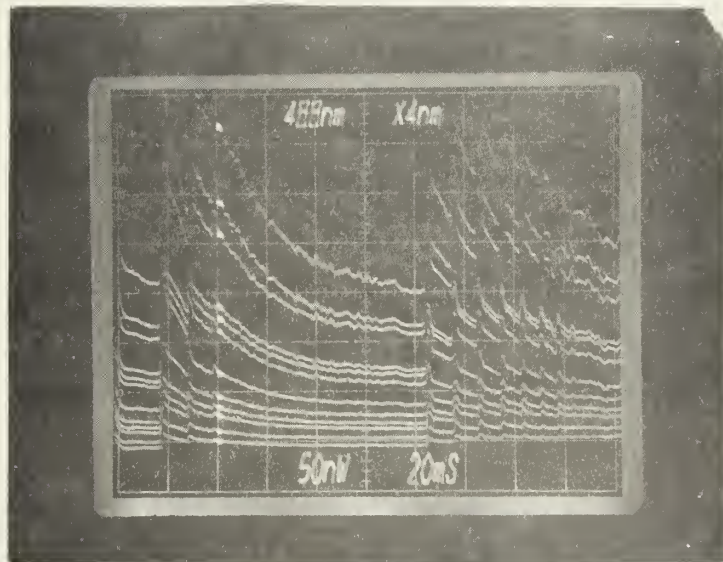


Figure 3b. Bandhead spectra for Aluminum Alloy 1100.

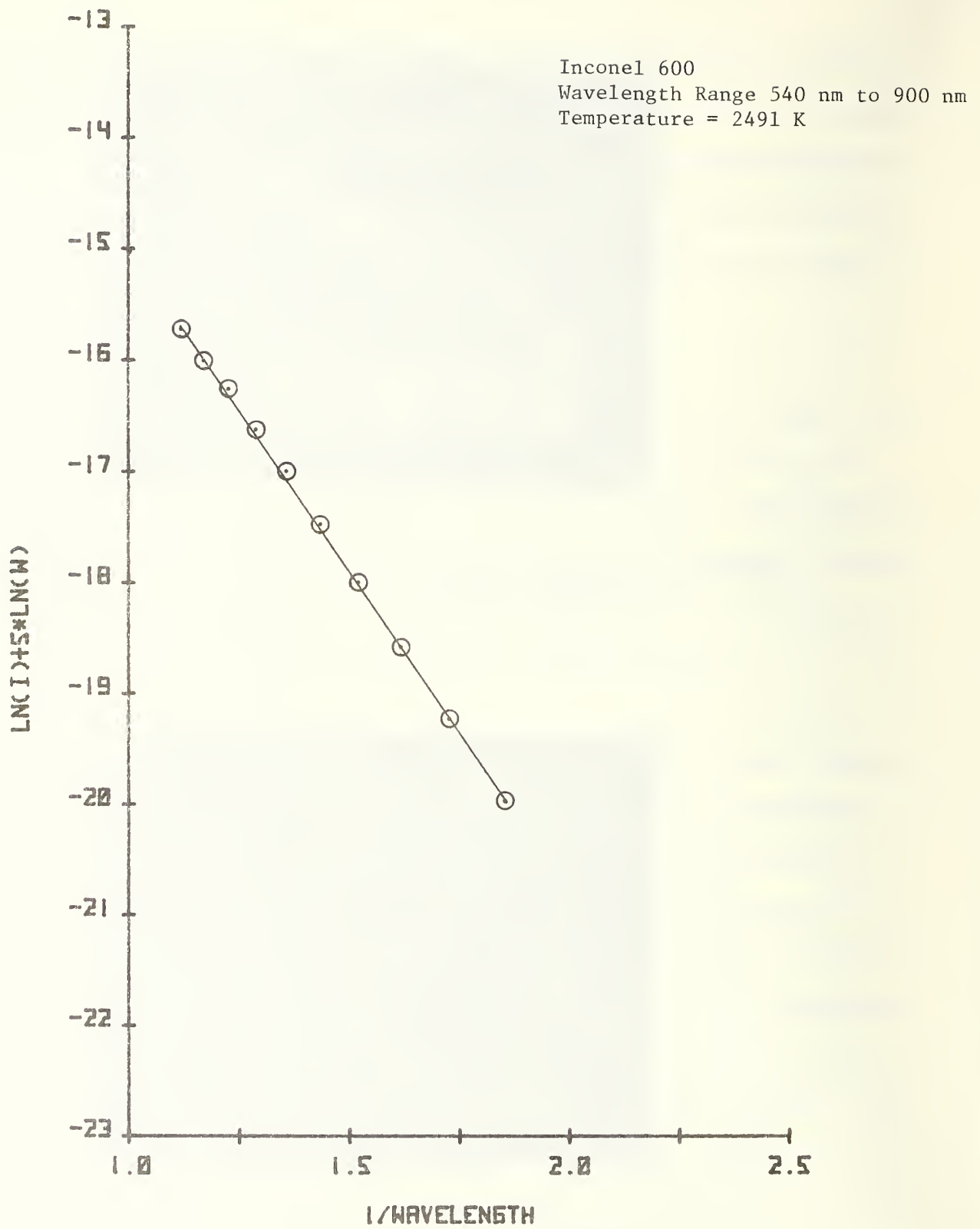


Figure 4. Graph of thermal emission spectrum for temperature determination

Tensile-50 Aluminum Alloy  
Wavelength Range 600 nm to 800 nm  
Temperature = 3348 K

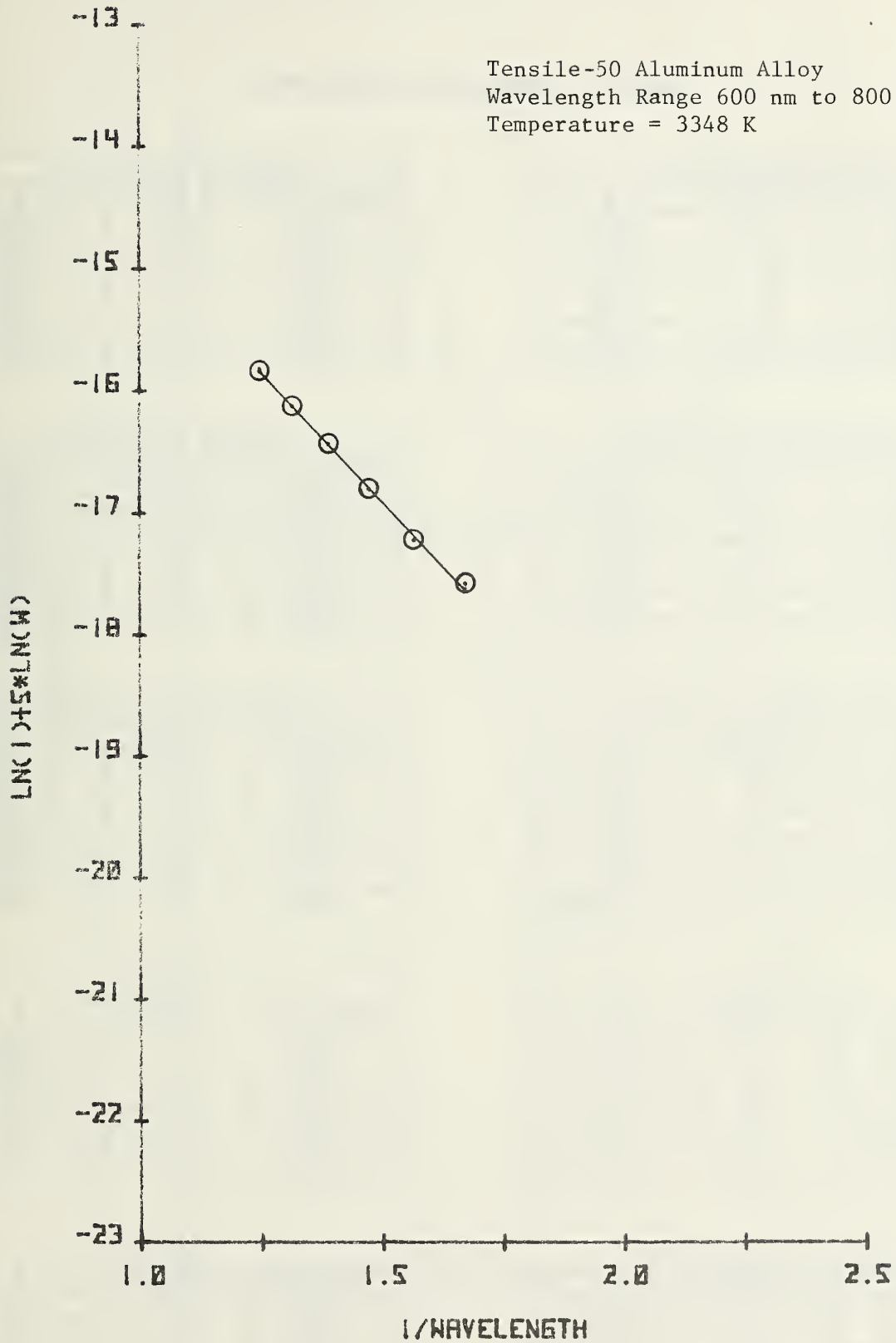


Figure 5. Graph of thermal emission spectrum for temperature determination.

TABLE 3: COMBUSTION TEMPERATURES

304 Stainless Steel		
Temp., K	± Temp.	± %
2558	19	0.72
2497	45	1.82
2690	14	0.52
2628	25	0.96
2645	10	0.39
2689	35	1.28

Aluminum Alloy 2219		
Temp., K	± Temp.	± %
3327	102	3.06
3515	62	1.77
3469	65	1.86
3452	42	1.20
3275	71	2.17
3430	40	1.17

347 Stainless Steel		
Temp., K	± Temp.	± %
2545	27	1.07
2699	28	1.02
2487	18	0.74
2520	20	0.78
2690	17	0.62
2732	39	1.42

Aluminum Alloy 6061		
Temp., K	± Temp.	± %
3400	78	2.30
3271	80	2.46
3534	40	1.13
3303	87	2.63
3282	51	1.56
3041	59	1.94

21-6-9 Stainless Steel		
Temp., K	± Temp.	± %
2520	12	0.47
2470	32	1.31
2630	21	0.80
2553	27	1.04
2629	16	0.61
2678	28	1.05

Aluminum Alloy Tensile-50		
Temp., K	± Temp.	± %
3348	77	2.29
3456	49	1.41
3408	79	2.32
3318	60	1.81
3451	81	2.34
3462	48	1.38

Inconel		
Temp., K	± Temp.	± %
2513	16	0.65
2491	23	0.91
2527	30	1.17
2631	33	1.24
2579	13	0.49
2642	30	1.14

Bronze		
Temp., K	± Temp.	± %
2072	15	0.72
2105	17	0.80
2202	15	0.70
2192	13	0.61
2244	14	0.64
2173	16	0.75

Aluminum Alloy 1100		
Temp., K	± Temp.	± %
3607	71	1.96
3731	59	1.57
3513	84	2.40
3499	37	1.05
3331	63	1.90
3392	43	1.28

BeCu		
Temp., K	± Temp.	± %
2441	23	0.96
2497	11	0.45
2839	17	0.59
2533	22	0.86
2720	14	0.53
2479	19	0.76

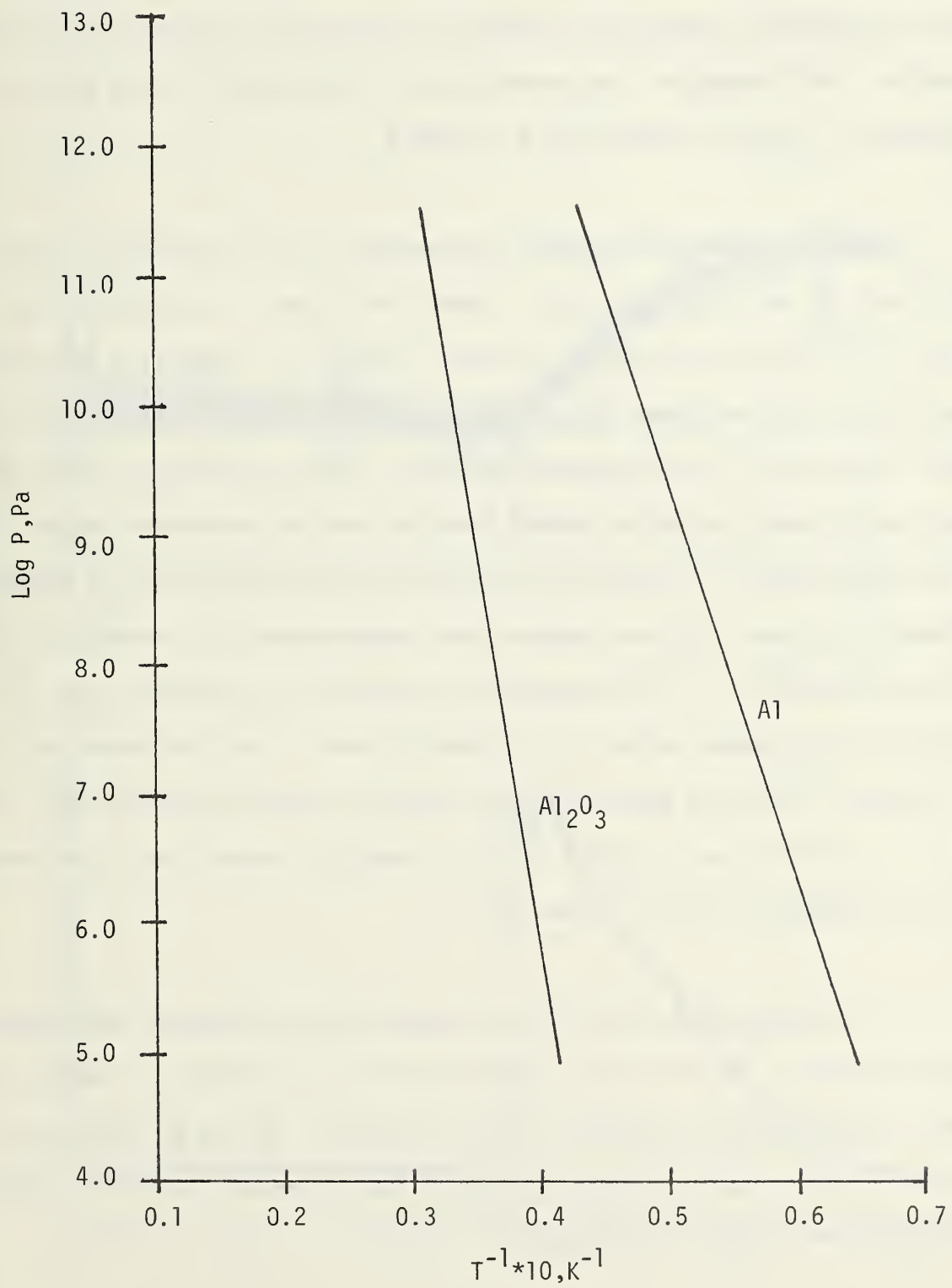


Figure 6. Vapor pressure of Al and  $Al_2O_3$ .

studied. This temperature could not be confirmed since the RSS presently cannot differentiate between the combustion zone and the surface of the molten sample. The combustion zone temperatures, as determined by the procedure of Appendix A, ranged between 3000 K to 3700 K.

Figures 7a, 10a, 13a and 16a show examples of the weight gain curves obtained for each aluminum alloy. These curves show a nonstoichiometric weight gain. There are three reasons for this. First, the combustion was generally slightly incomplete, less than 1 percent; alloy particles were present on or near the bottom of the combustion residue. Second, microscopic oxide particles and some ejected particles escaped from the covered combustion region. Third, the weight sensor is temperature sensitive and this shows up as a weight loss. Overall the final indicated weights were approximately 80 percent to 90 percent of stoichiometric. If the assumption is made that the material lost is proportional to the weight gained - only oxide is lost - then the curves can be used to construct plots of weight of alloy burned or remaining versus time. Figures 8, 11, 14 and 17 show fraction of alloy remaining versus time curves constructed from Figures 7a, 10a, 13a and 16a.

The combustion kinetics for our experimental arrangement were thought to be first-order. To show this, logarithmic plots of fraction of alloy remaining versus time were made, Figures 9, 12, 15, and 18. As can be seen there are one or more linear regions indicating first-order or nearly first-order combustion kinetics for the experimental setup.

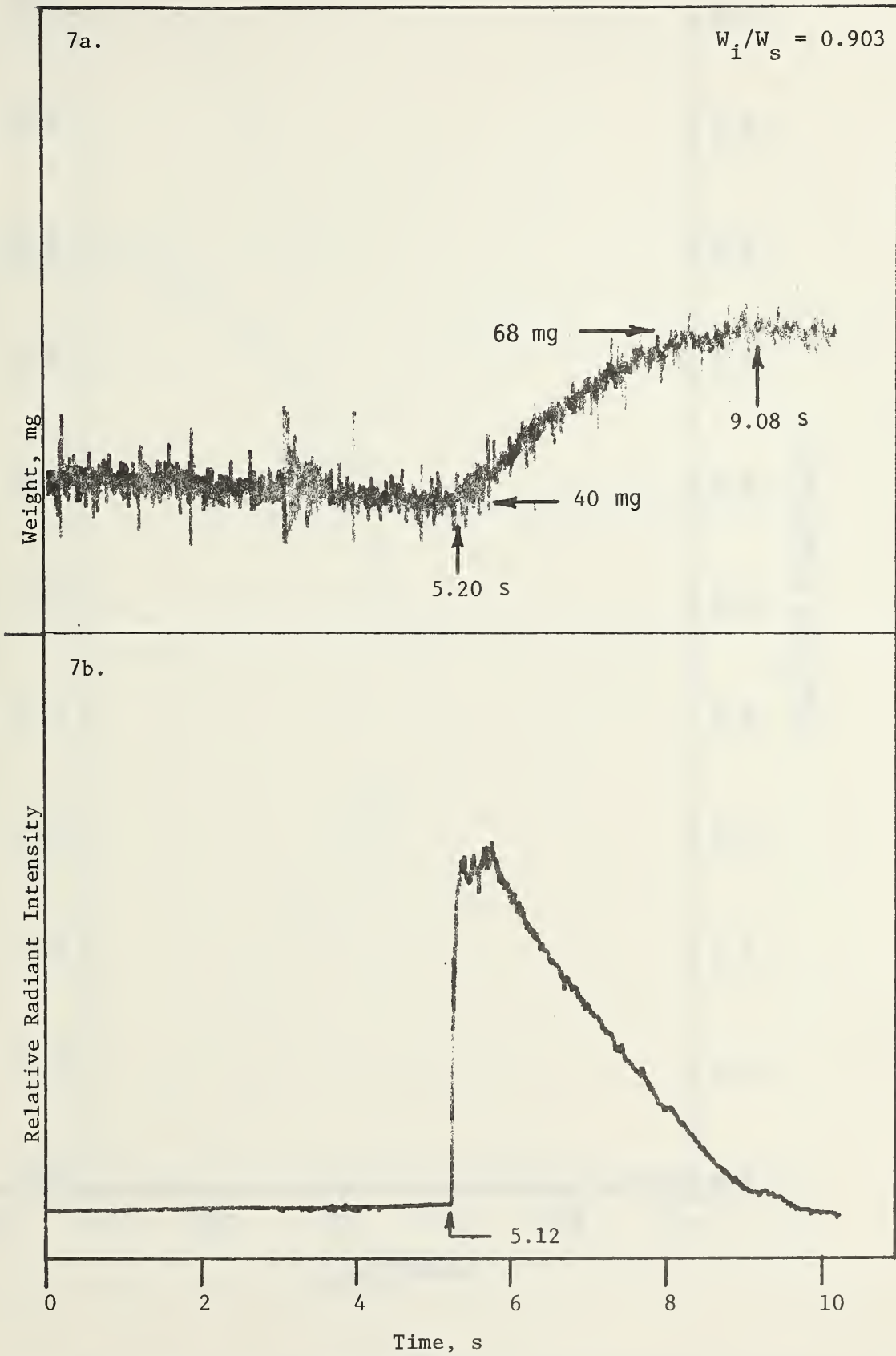


Figure 7. 1100 Aluminum Alloy combustion rate and radiant intensity

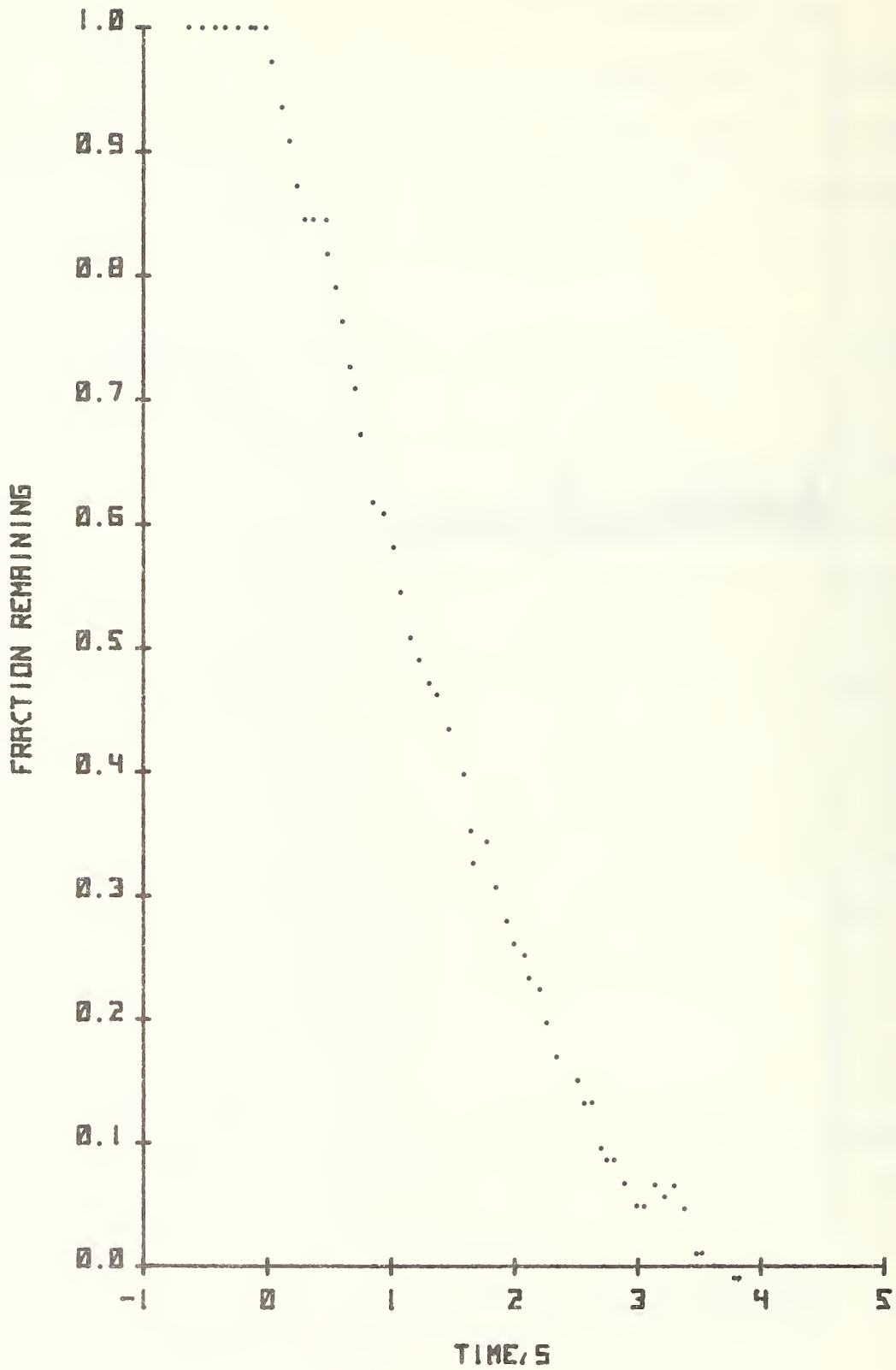


Figure 8. Fraction of 1100 Aluminum Alloy remaining during combustion.

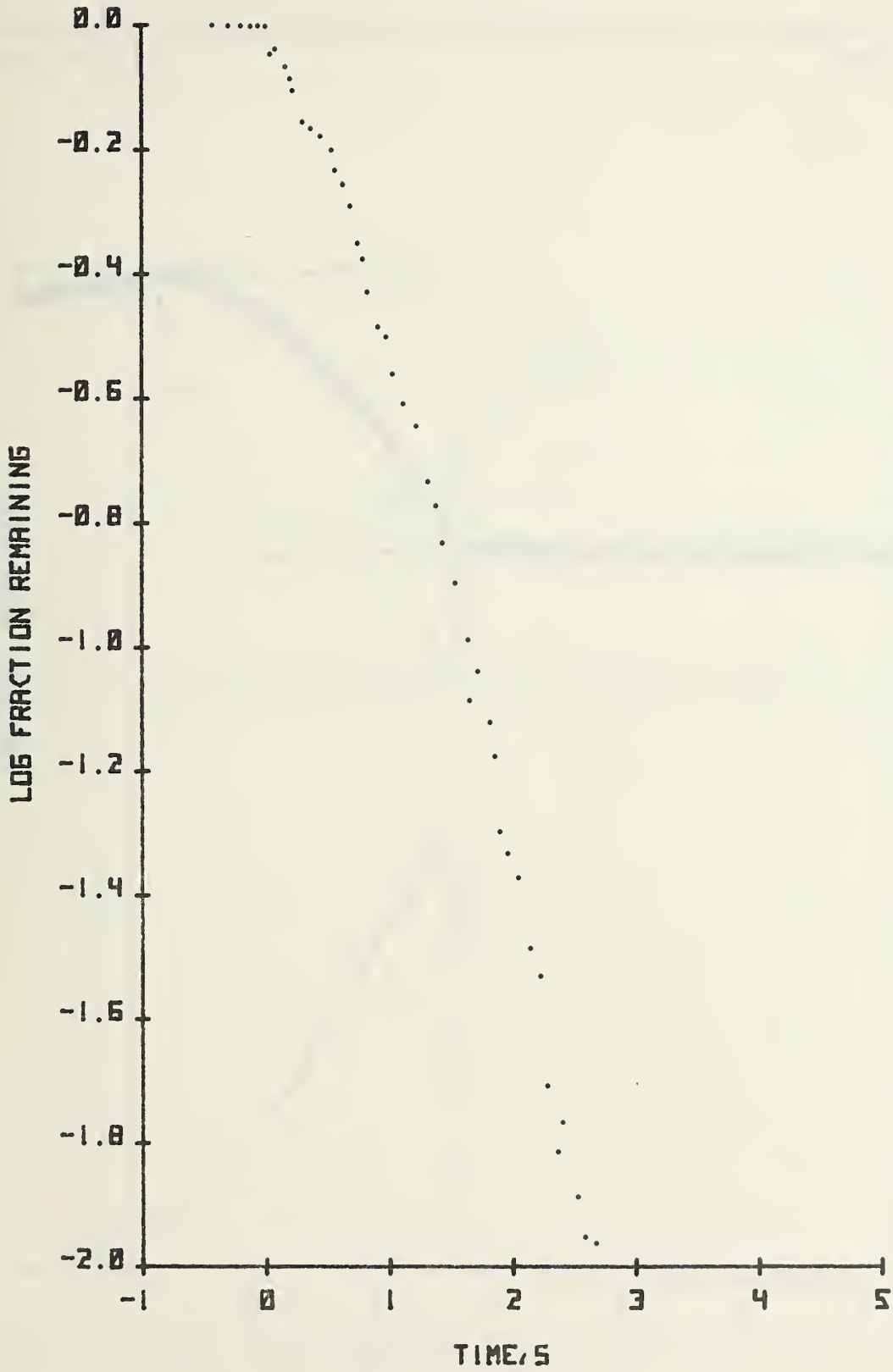


Figure 9. Log fraction remaining for 1100 Aluminum Alloy.

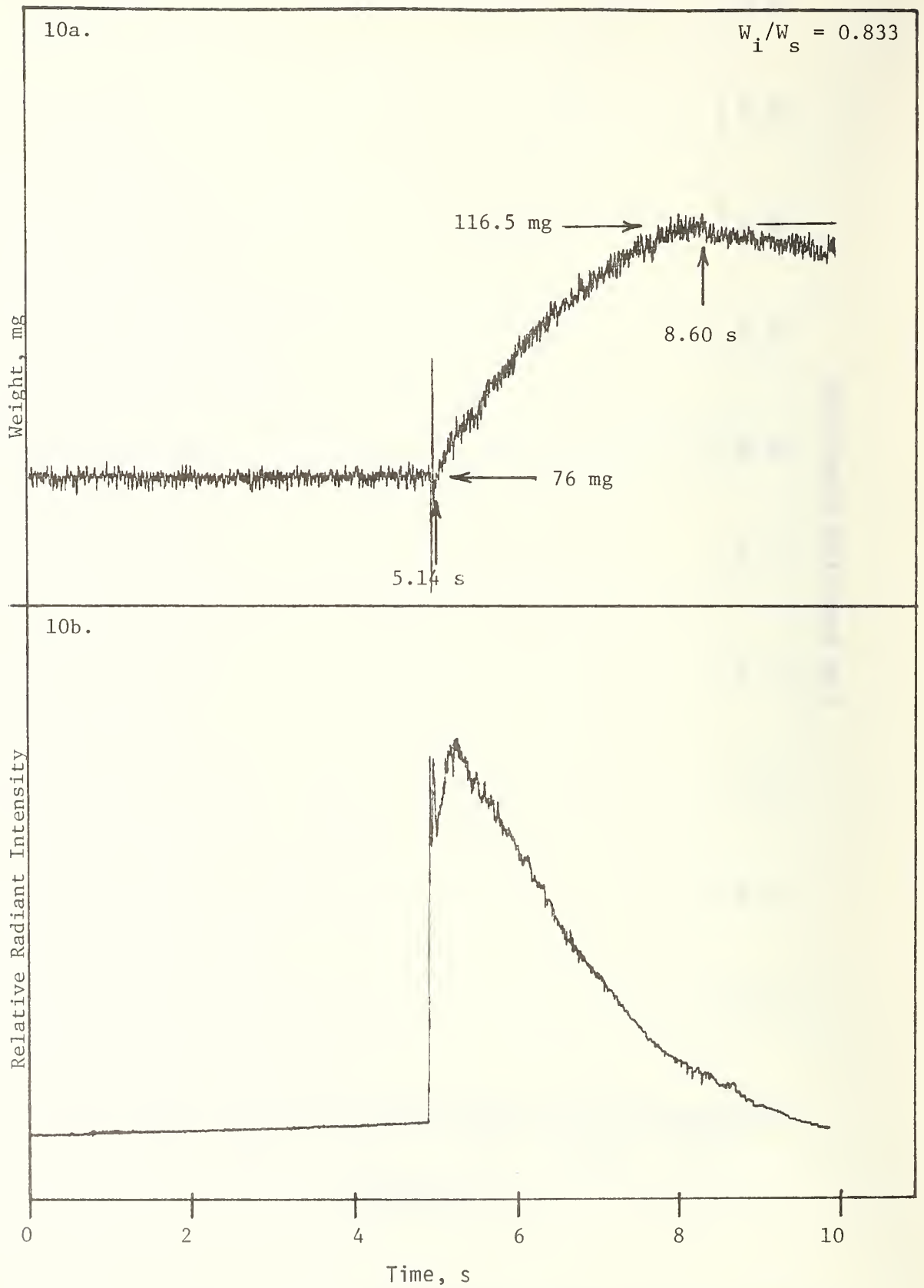


Figure 10. 2219 Aluminum Alloy combustion rate and radiant intensity.

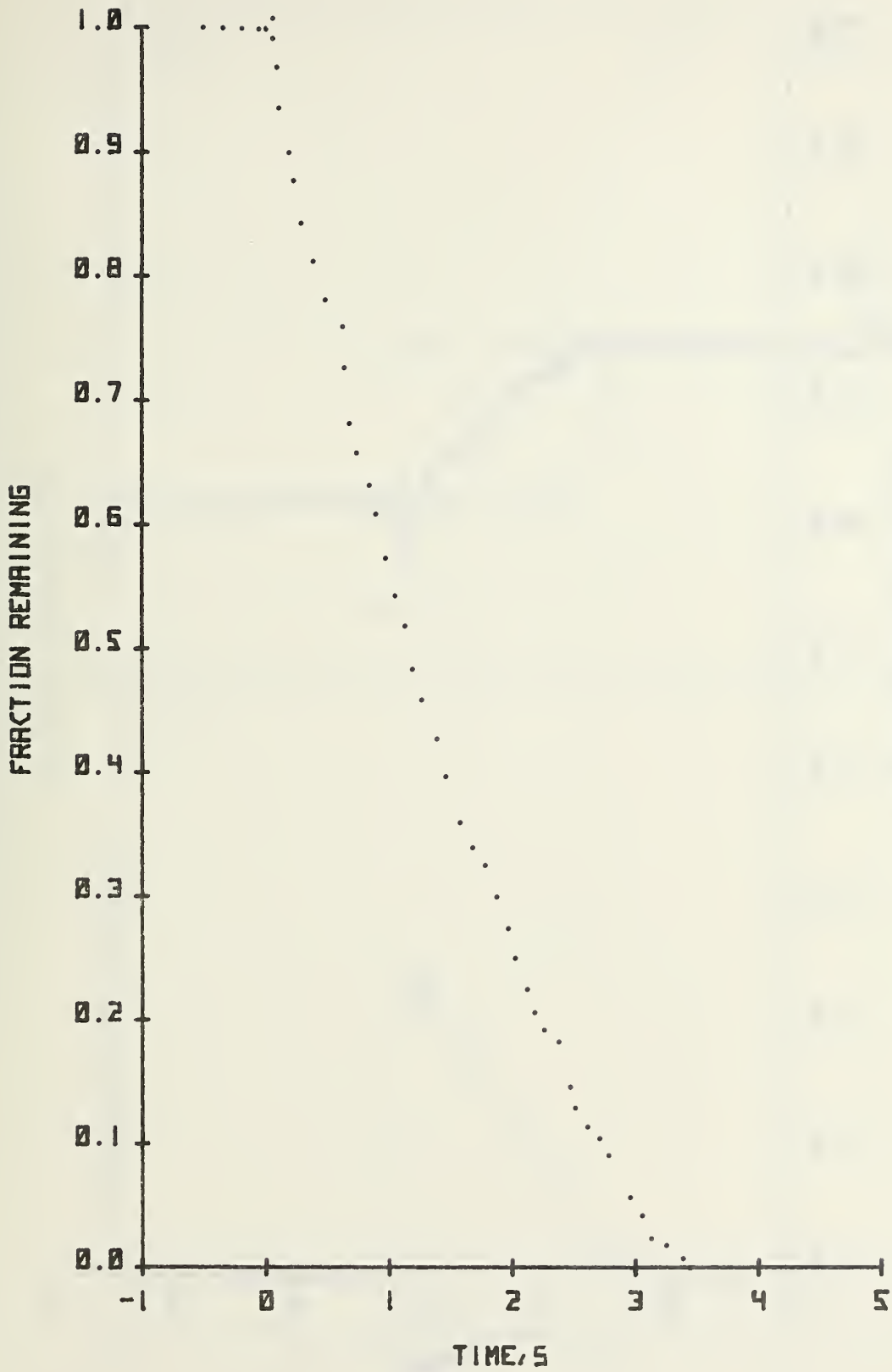


Figure 11. Fraction of 2219 Aluminum Alloy remaining during combustion.

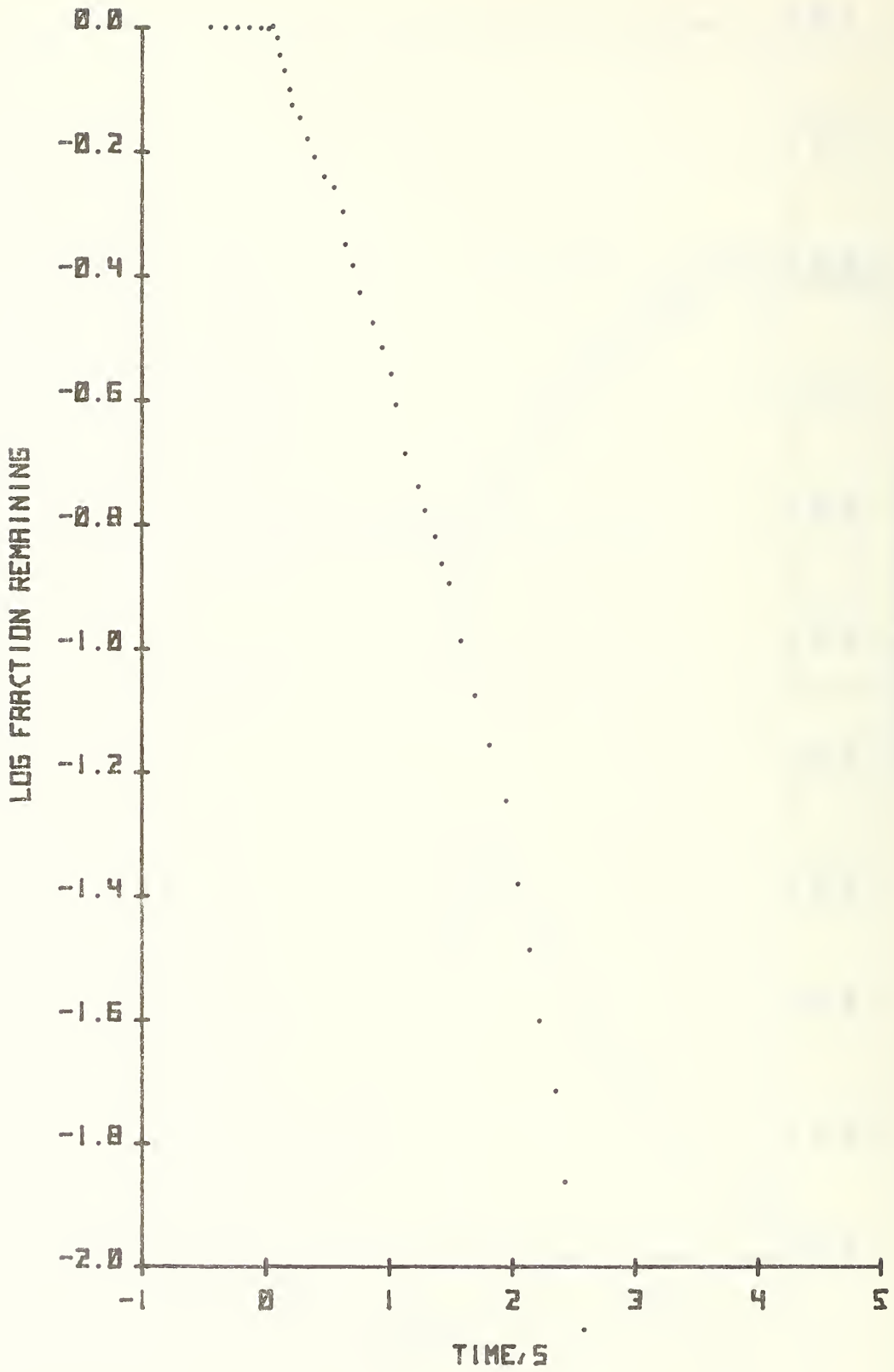


Figure 12. Log fraction remaining for 2219 Aluminum Alloy.

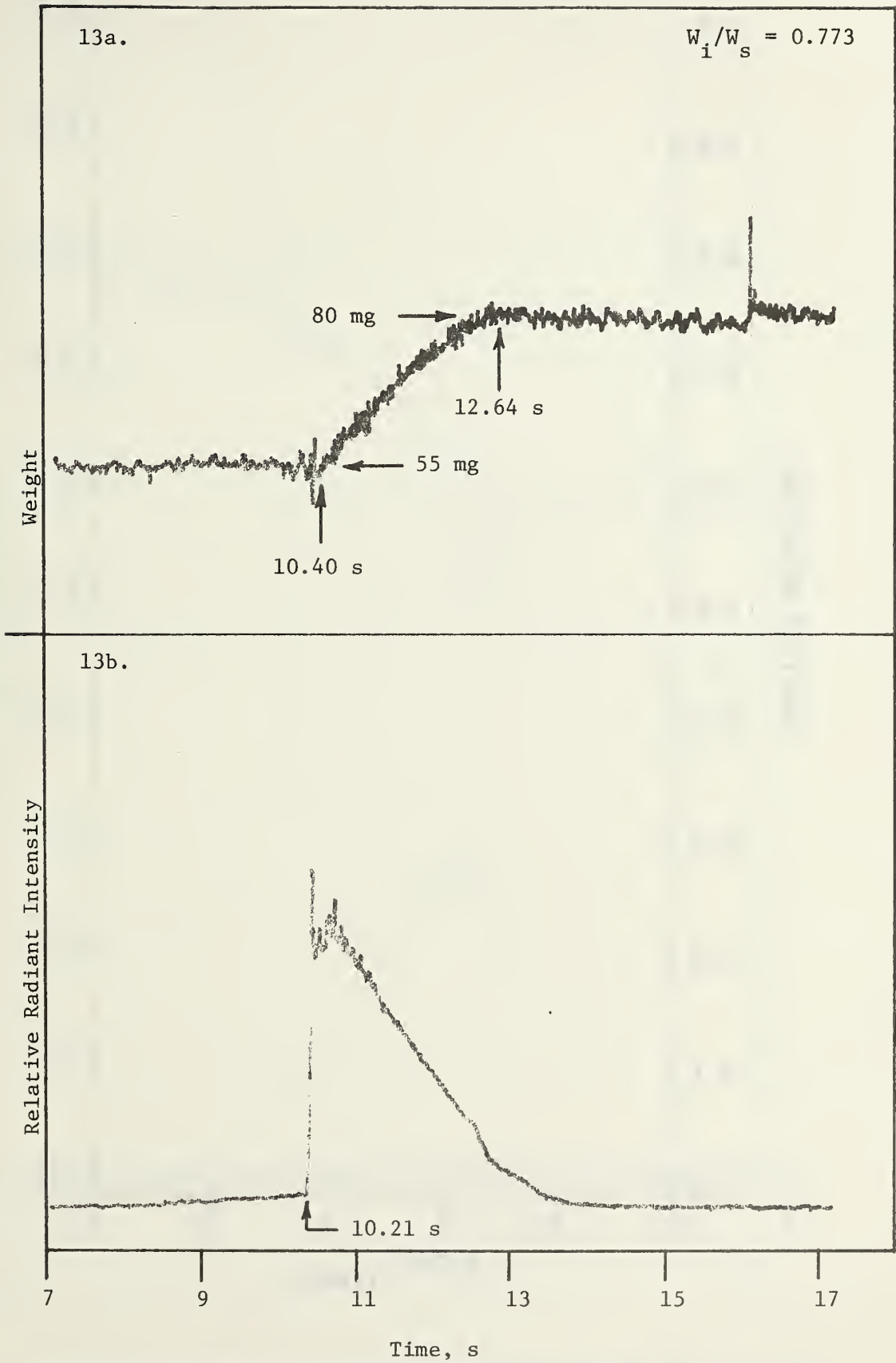


Figure 13. 6061 Aluminum Alloy combustion rate and radiant intensity.

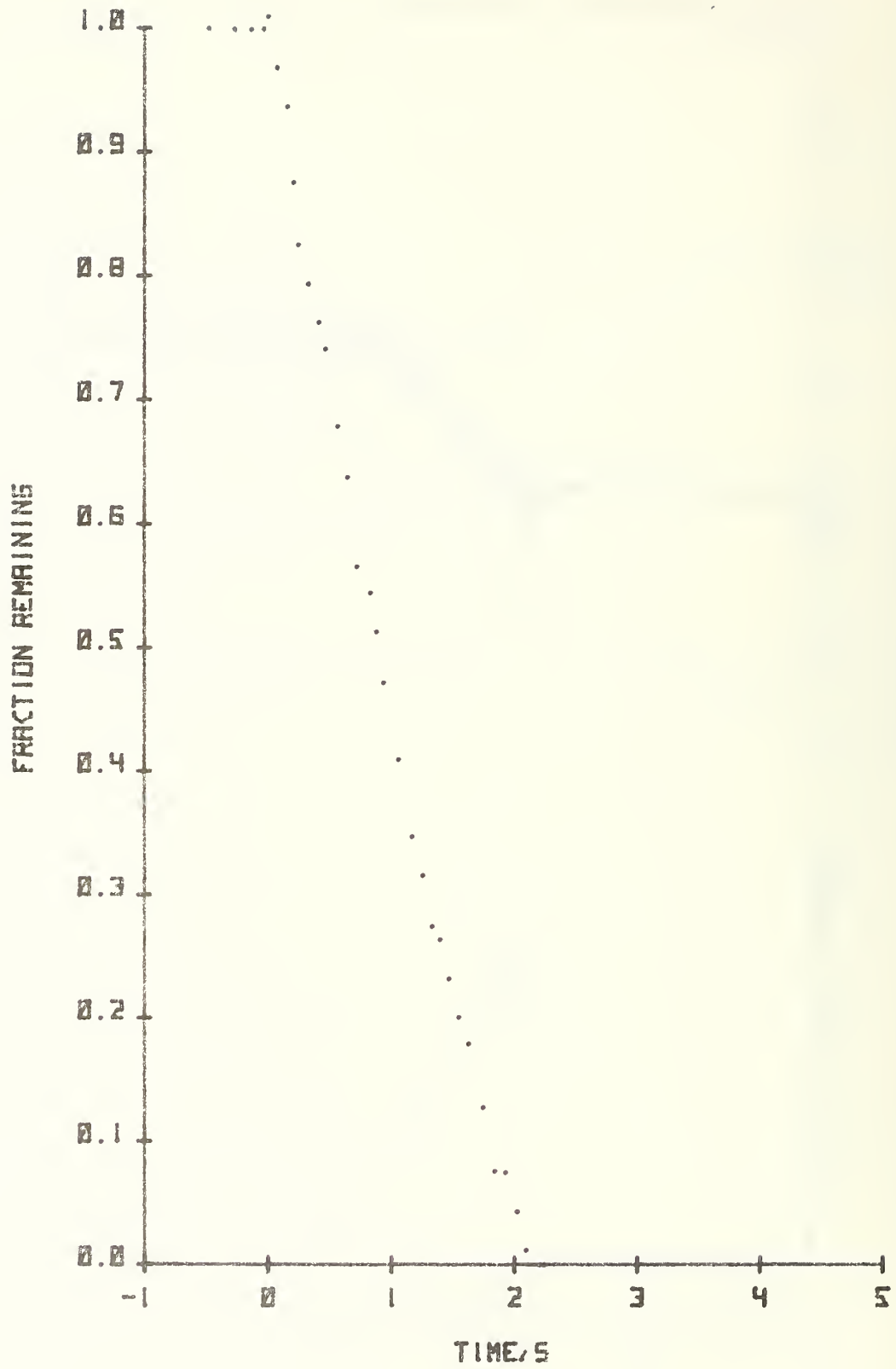


Figure 14. Fraction of 6061 Aluminum Alloy remaining during combustion.

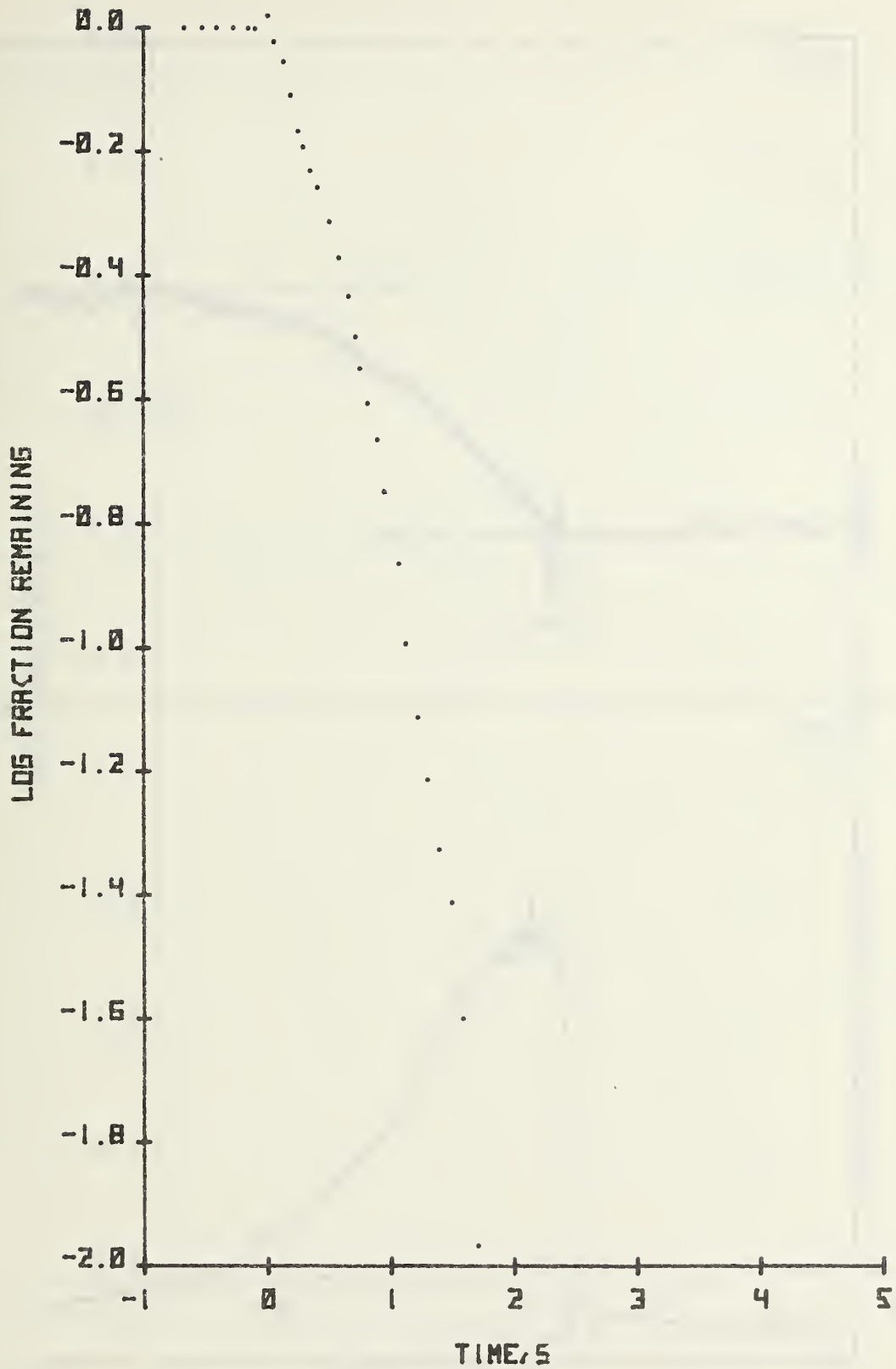


Figure 15. Log fraction remaining for 6061 Aluminum Alloy.

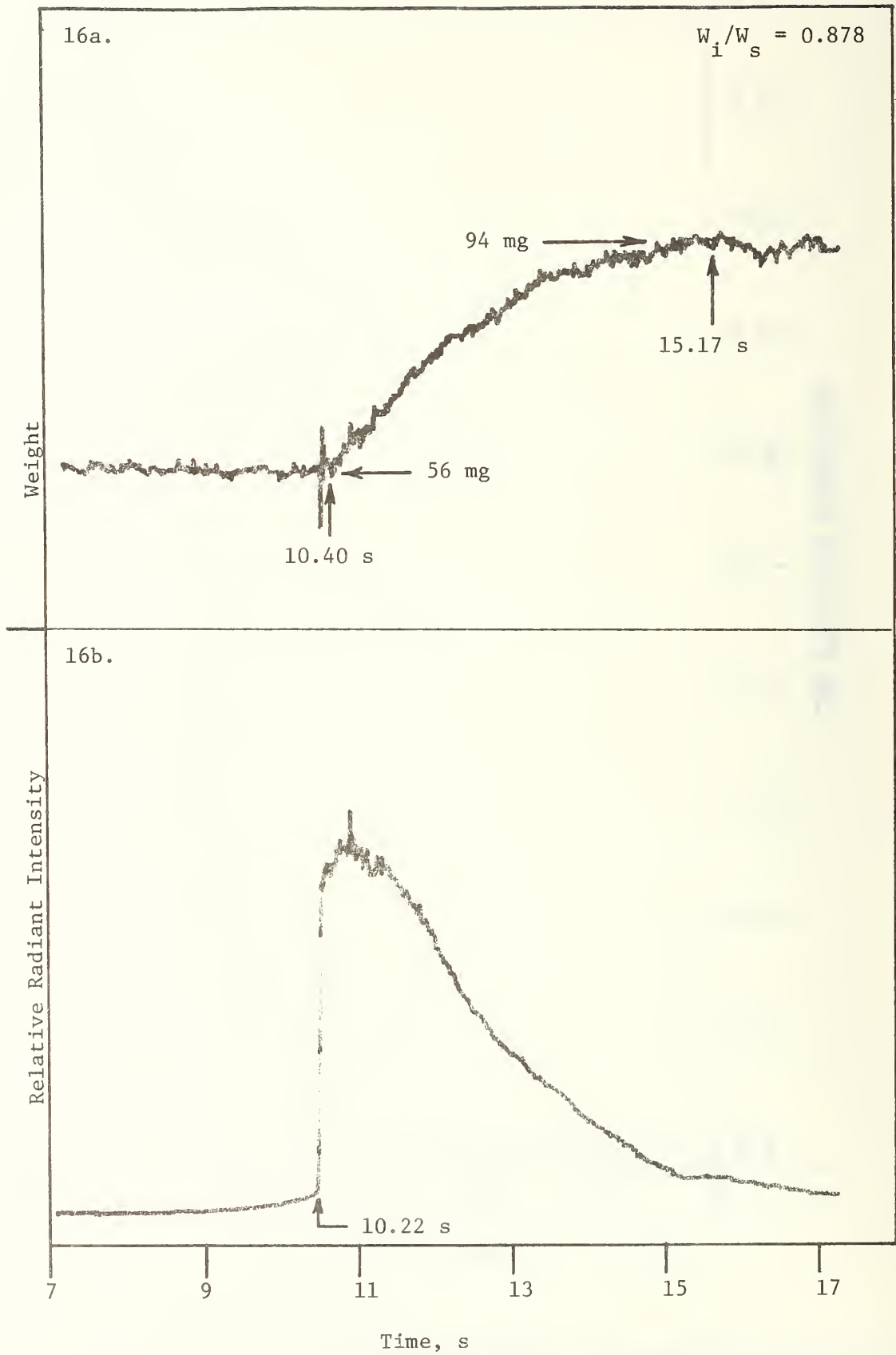


Figure 16. Tensile-50 Aluminum Alloy combustion rate and radiant intensity.

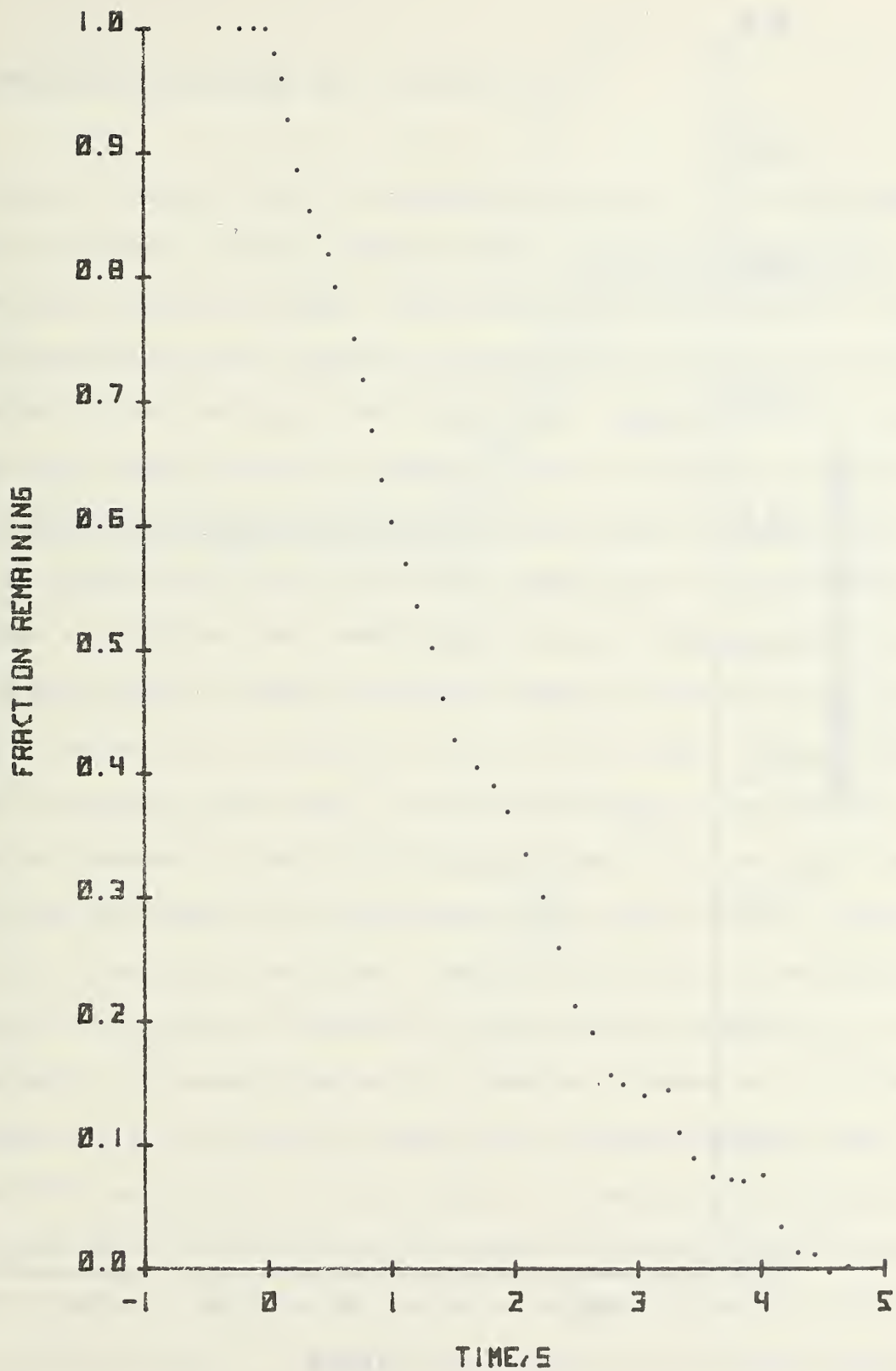


Figure 17. Fraction of Tensile-50 Aluminum Alloy remaining during combustion.

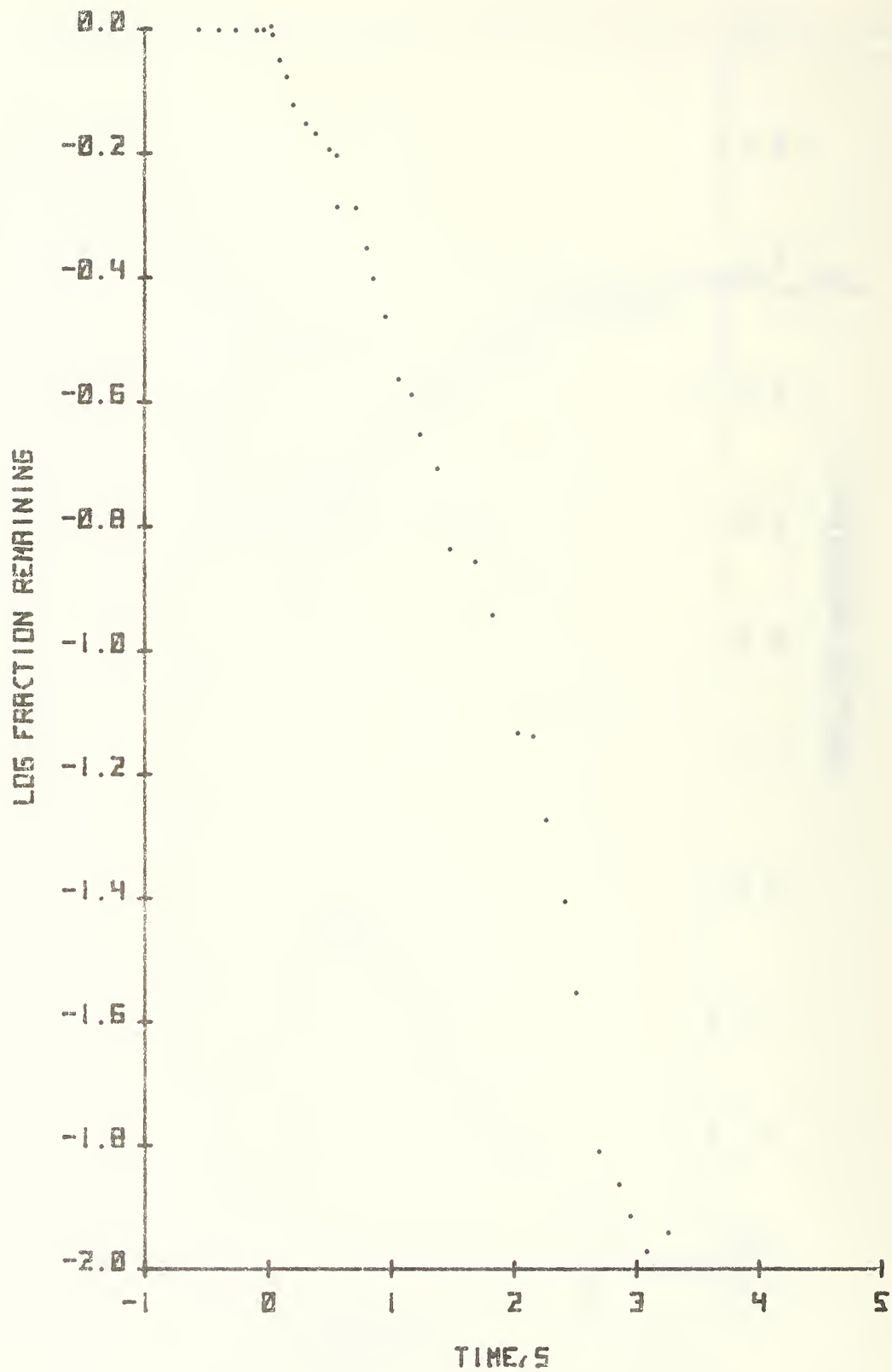


Figure 18. Log fraction remaining for Tensile-50 Aluminum Alloy.

## B. Stainless Ferrous Alloys 304, 347 and 21-6-9

The three ferrous alloys had essentially the same ignition and combustion characteristics and, like the aluminum alloys, the combustion sequence can be divided into the same two stages. The alloys were usually difficult to ignite and had somewhat irregular combustion characteristics as evidenced by the radiant intensity curves of Figures 19b, 22b and 25b. Regardless of the variation in combustion intensity over the combustion period the alloys generally had two distinct combustion phases during the combustion stage. During the induction stage the samples would form a gray to black oxide layer. Ignition appears to begin when a combustion front, weak orange in color, advances, top to bottom, over the solid sample. However, this front appears to weaken momentarily; then a bright incandescence front forms at the top of the sample. Sample melting follows the advance of this front. The initial (orange) combustion zone appears as a shoulder on the radiant intensity curves, e.g. see Figure 19b. It has not been determined at this time whether some surface melting accompanies this initial combustion zone or not. Thus, it is not known at this time if the transition from oxidation to combustion takes place just before or at the alloy melting point. The second stage of the combustion sequence can be divided into two phases; the active combustion phase which is characterized by violent drop movement with the ejection of large droplets of material and a moderately active phase which is characterized by minimal drop activity and the ejection of small spray particles. The two phases are separated by a short period of greatly reduced activity. During the initial part of the combustion phase the surface tension of the drop is sufficient to form a well-defined sessile drop; however, in the latter part of the combustion phase the drop wets the graphite

surface and spreads out. There appears to be no liquid phase separation thus we conclude that the molten alloy and oxides are miscible or otherwise thoroughly mixed.

The combustion region was scanned with the RSS to determine if there were any emission lines which would indicate vapor reactions occurring. No emission lines in the 400 nm to 1100 nm spectral region were observed and no vapor reaction regions were observed on the movie film indicating no vapor-phase combustion was present. Temperatures calculated from spectral scans from 400 nm to 800 nm and 500 nm to 900 nm indicated maximum combustion temperatures between 2500 K and 2700 K, Table 3. Since no reacting vapor is considered to be present, the temperatures measured are those of the molten reacting material.

Weight-gain measurements were made in order to determine the combustion rate. Examples of typical results are shown in Figures 19a, 22a and 25a. As can be seen, the ejection of drops and spray by the burning sample is a complicating factor in obtaining an interpretable curve. However, these curves were used to generate fraction remaining and log fraction remaining curves, Figures 20, 21, 23, 24, 26, and 27. The best curves were obtained from 304 stainless steel. The overall combustion kinetics for the experimental setup, as determined from log plots, appear to be first-order with two distinct slopes. This change in slope may indicate a change in the oxidation mechanism and occurs when approximately one half of the sample is consumed.

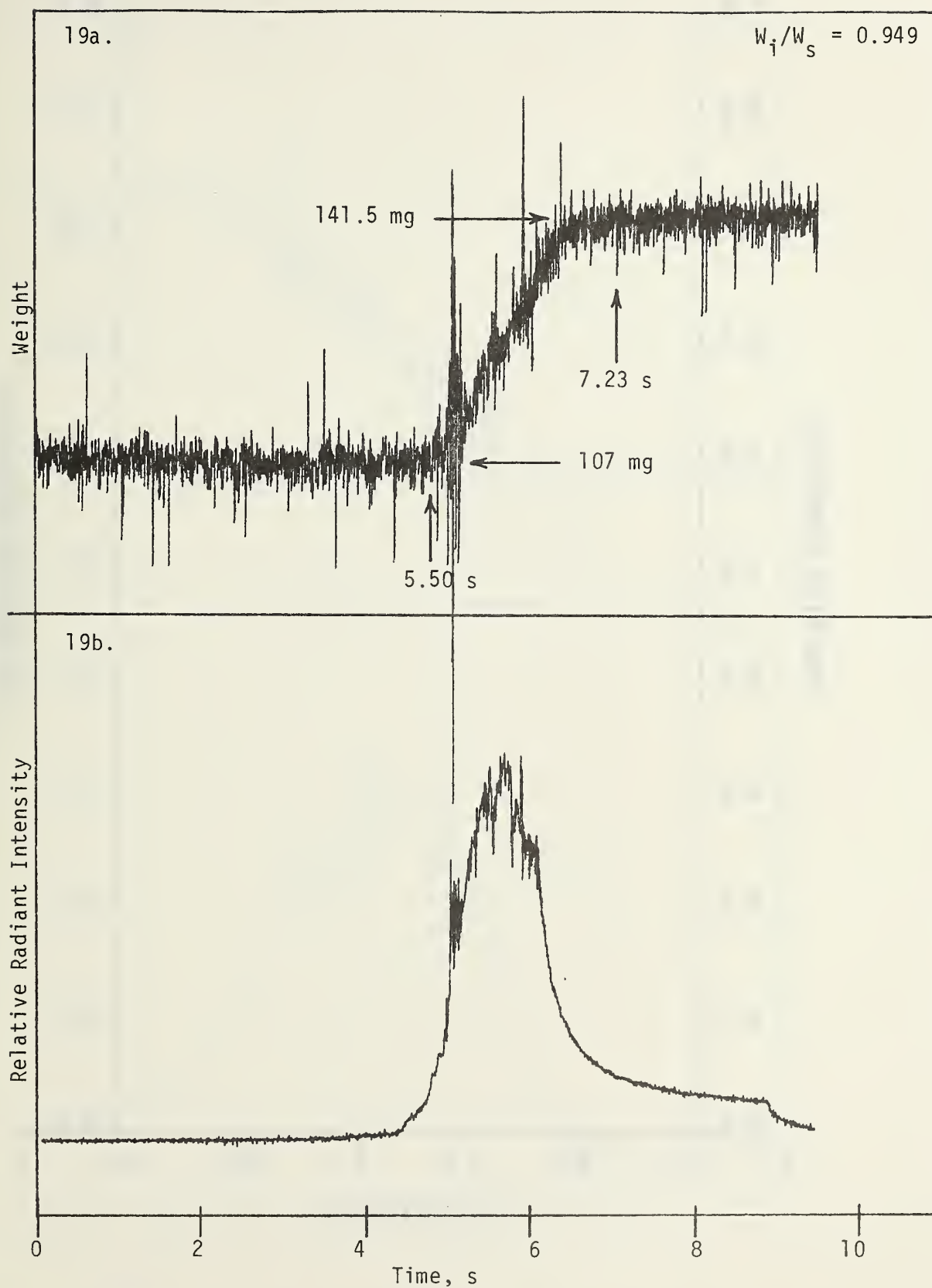


Figure 19. 304 Stainless Steel combustion rate and radiant intensity.

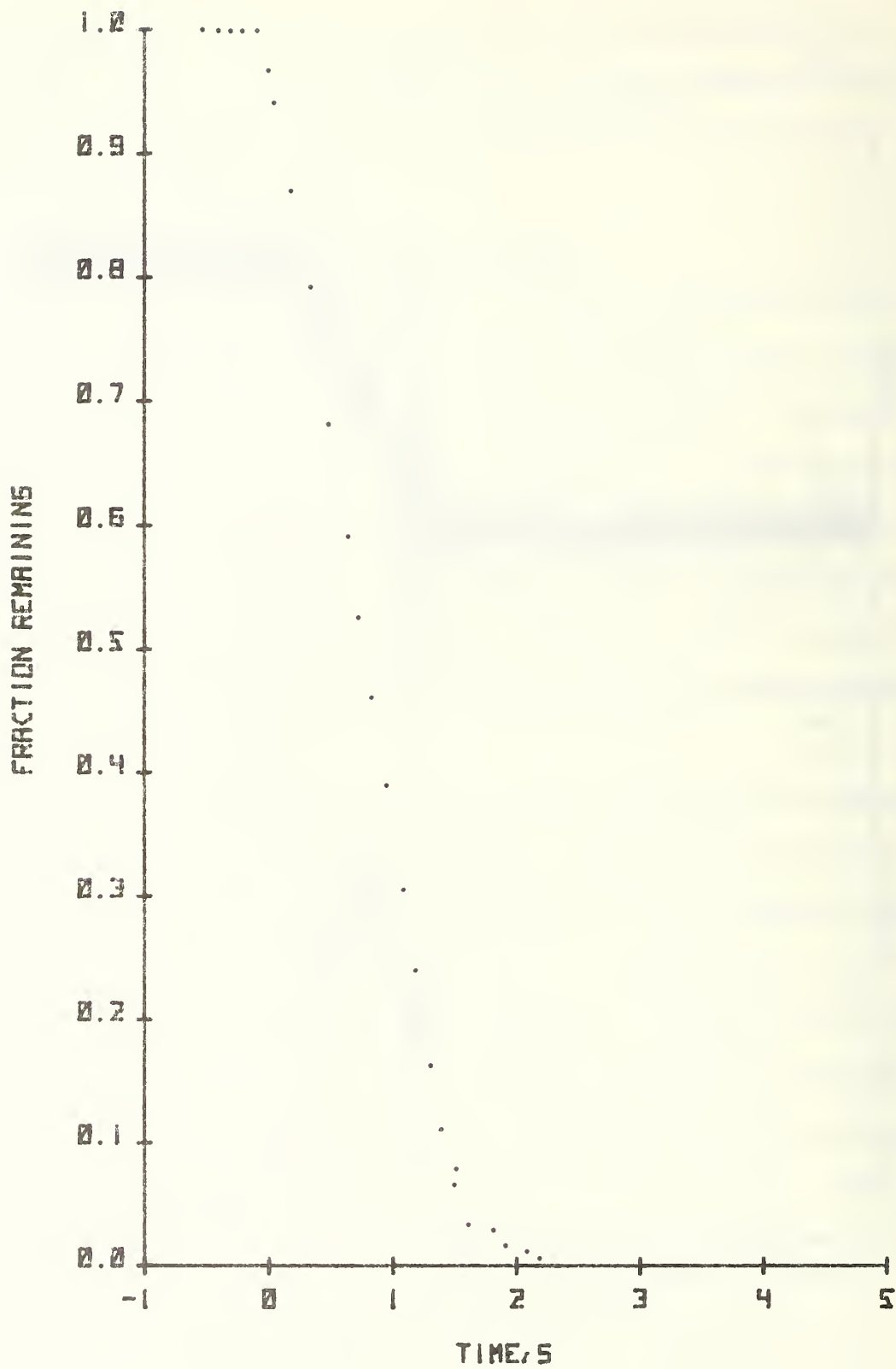


Figure 20. Fraction of 304 Stainless Steel remaining during combustion.

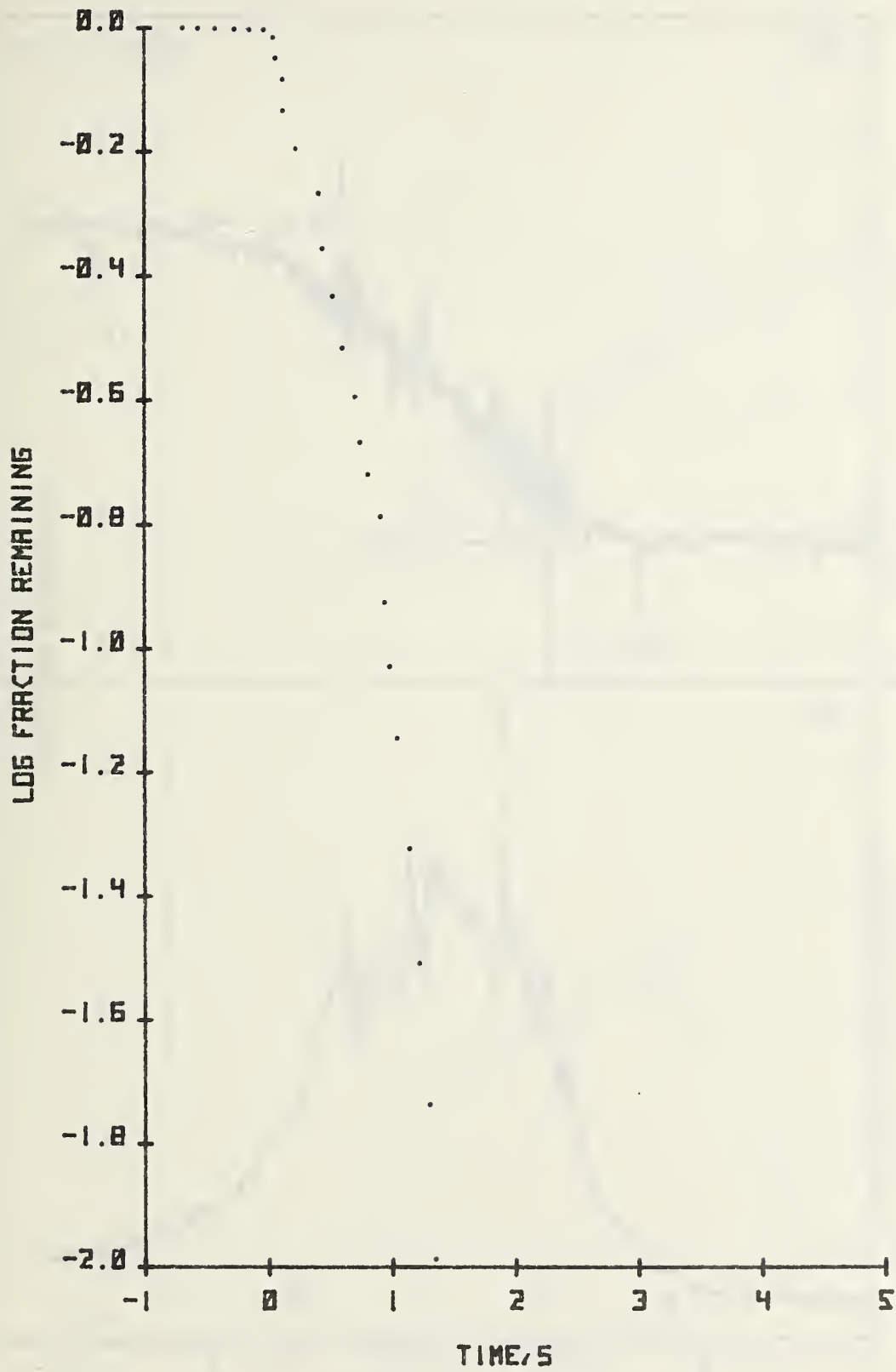


Figure 21. Log fraction remaining for 304 Stainless Steel.

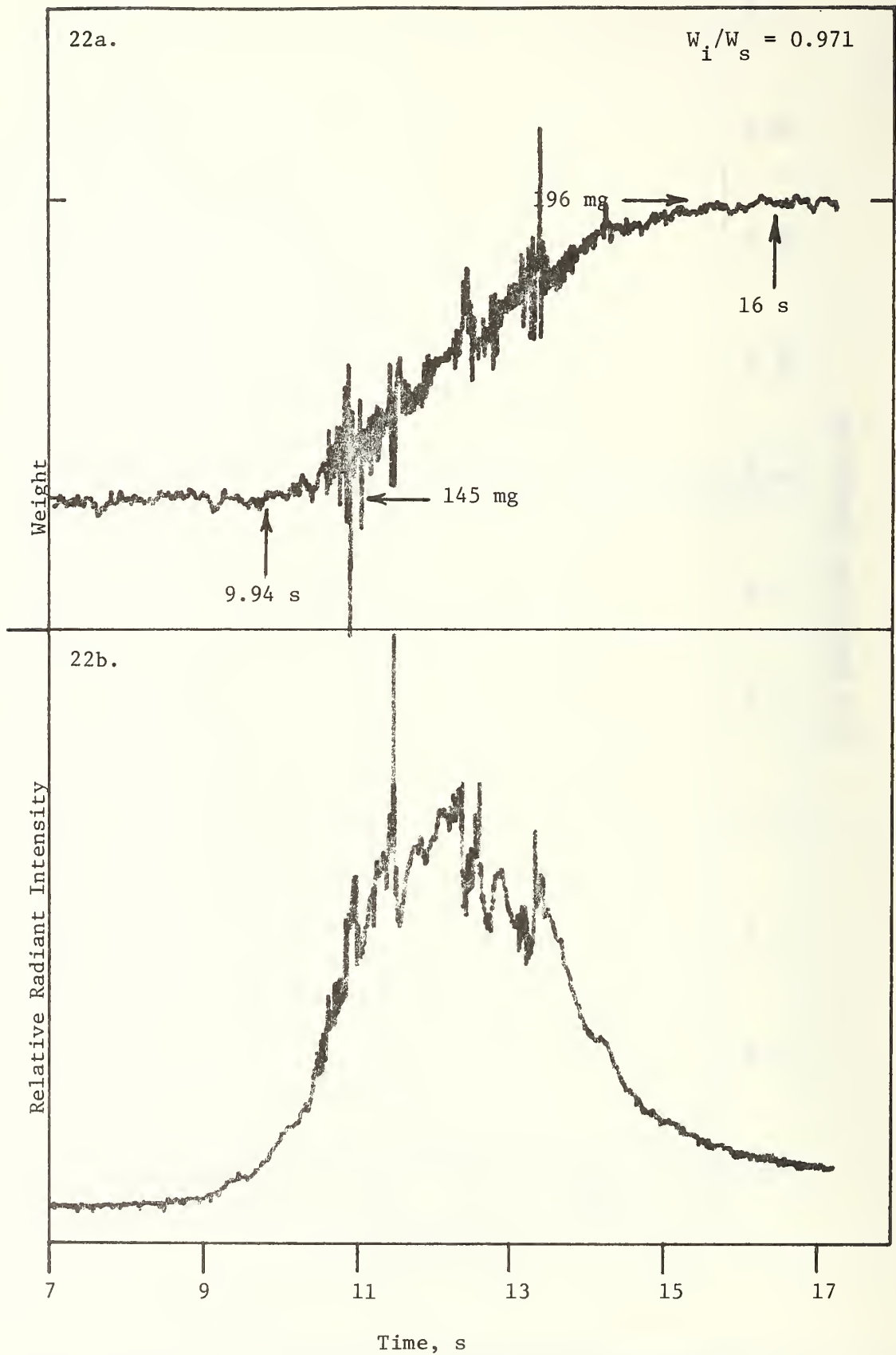


Figure 22. 347 Stainless Steel combustion rate and radiant intensity.

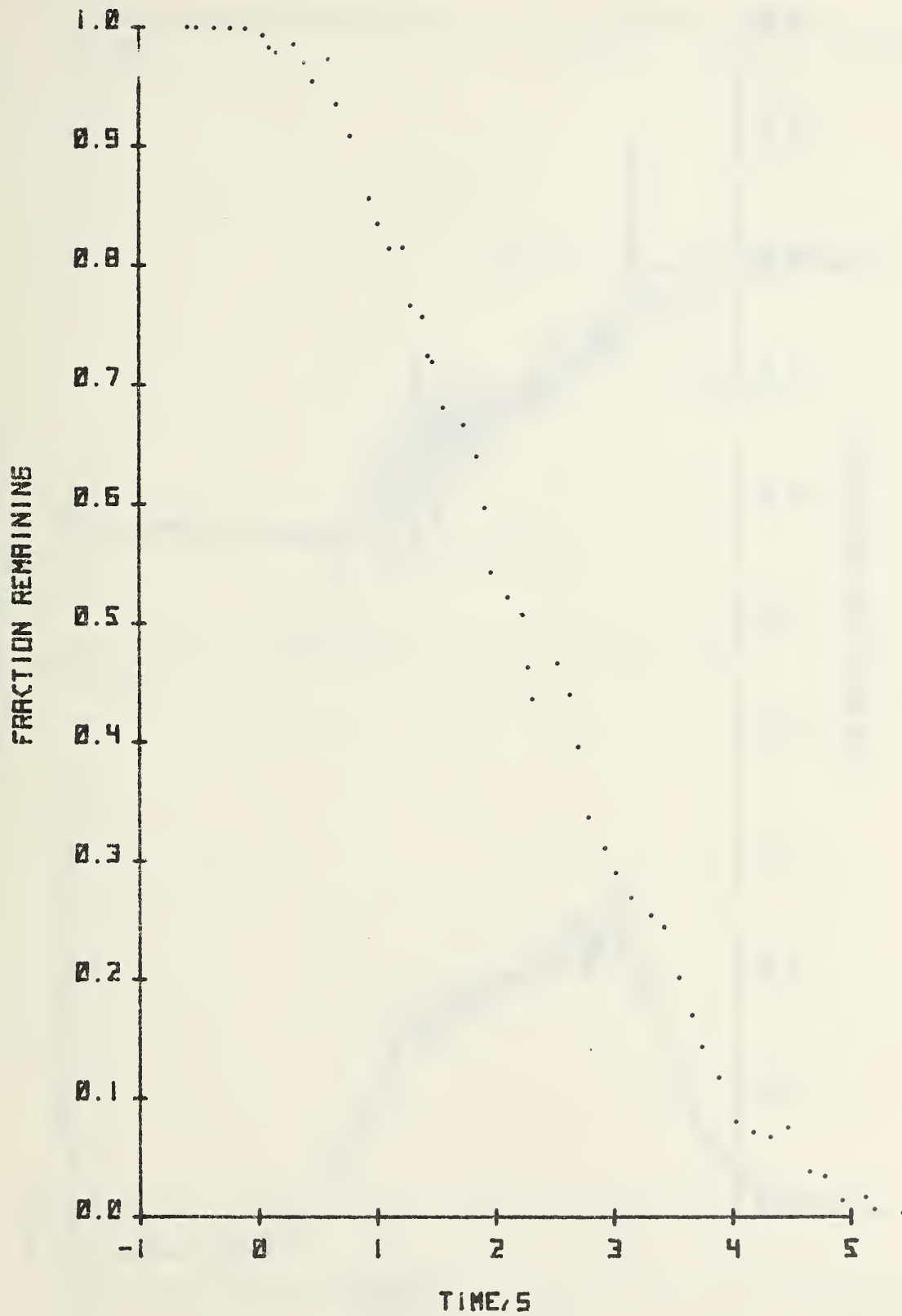


Figure 23. Fraction of 347 Stainless Steel remaining during combustion.

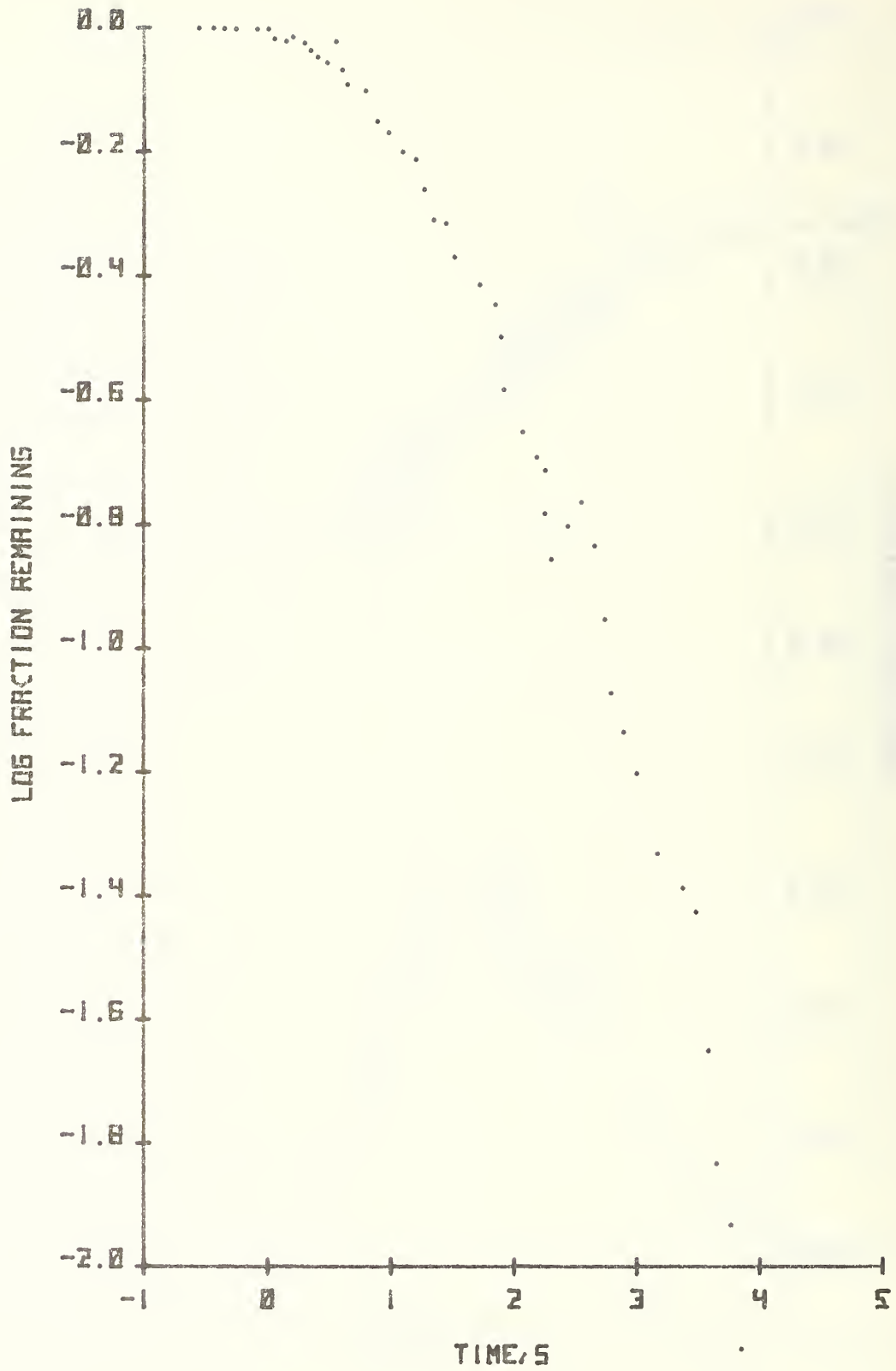


Figure 24. Log fraction remaining for 347 Stainless Steel.

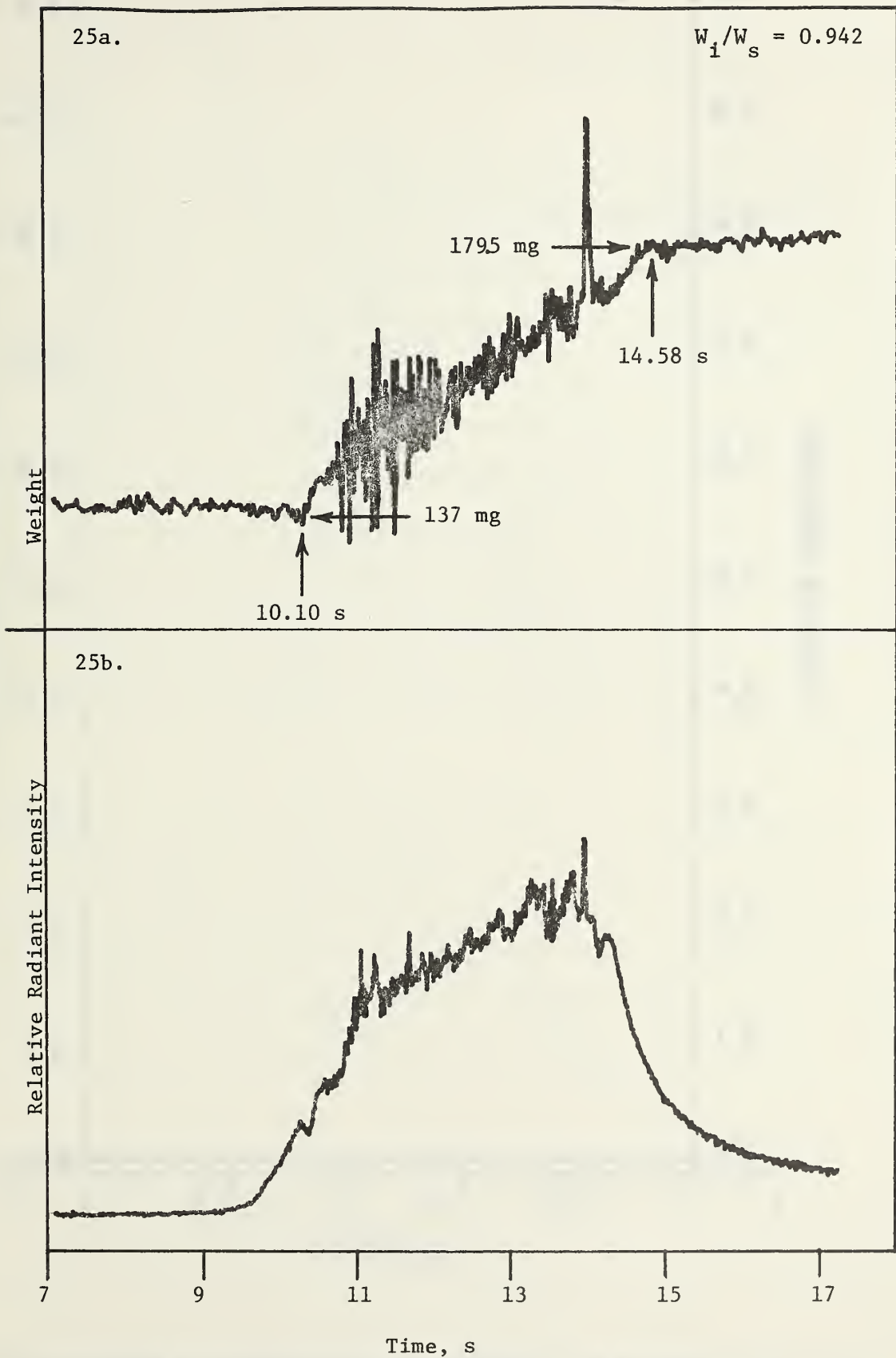


Figure 25. 21-6-9 Stainless Steel combustion rate and radiant intensity.

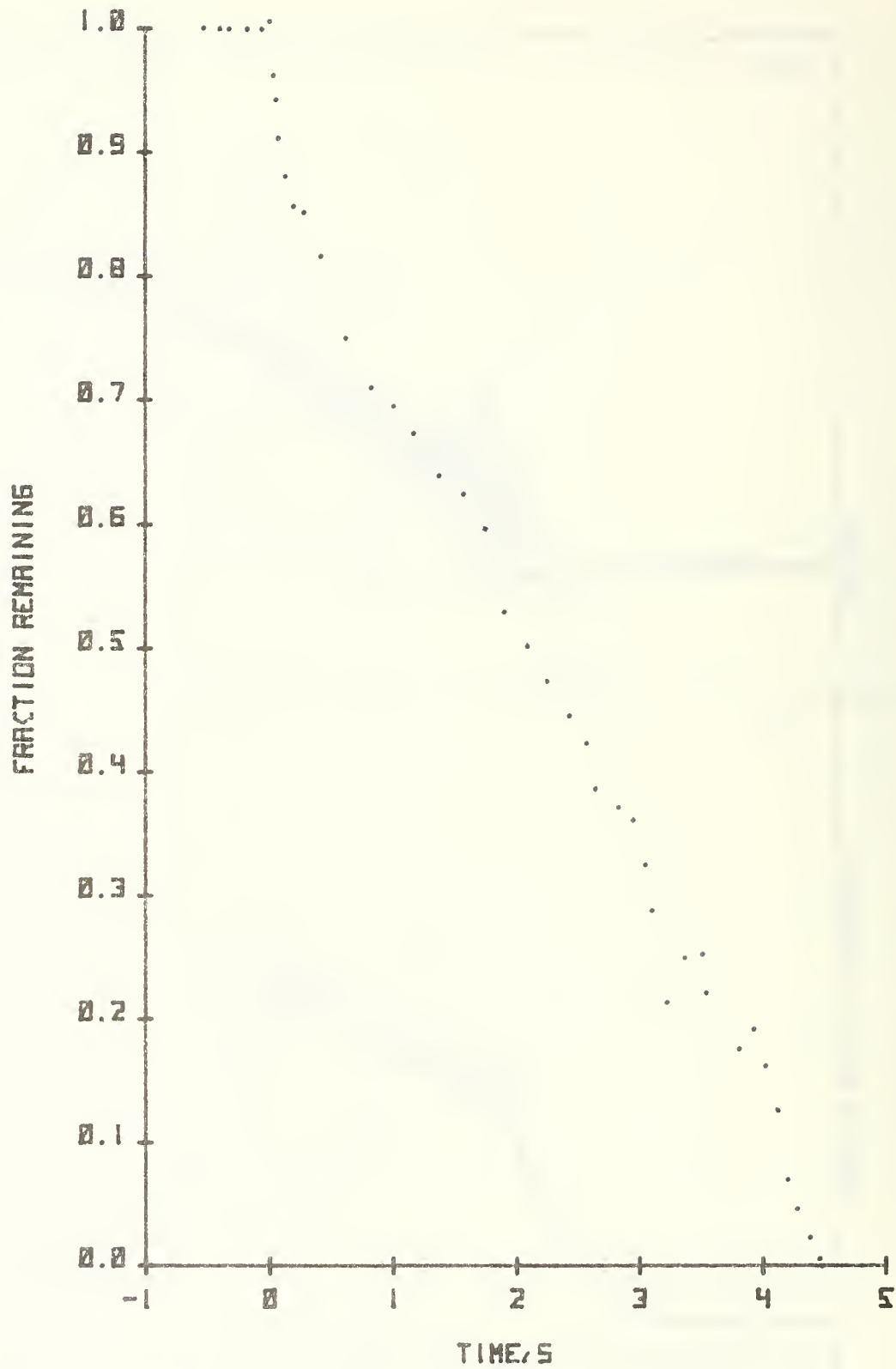


Figure 26. Fraction of 21-6-9 Stainless Steel remaining during combustion.

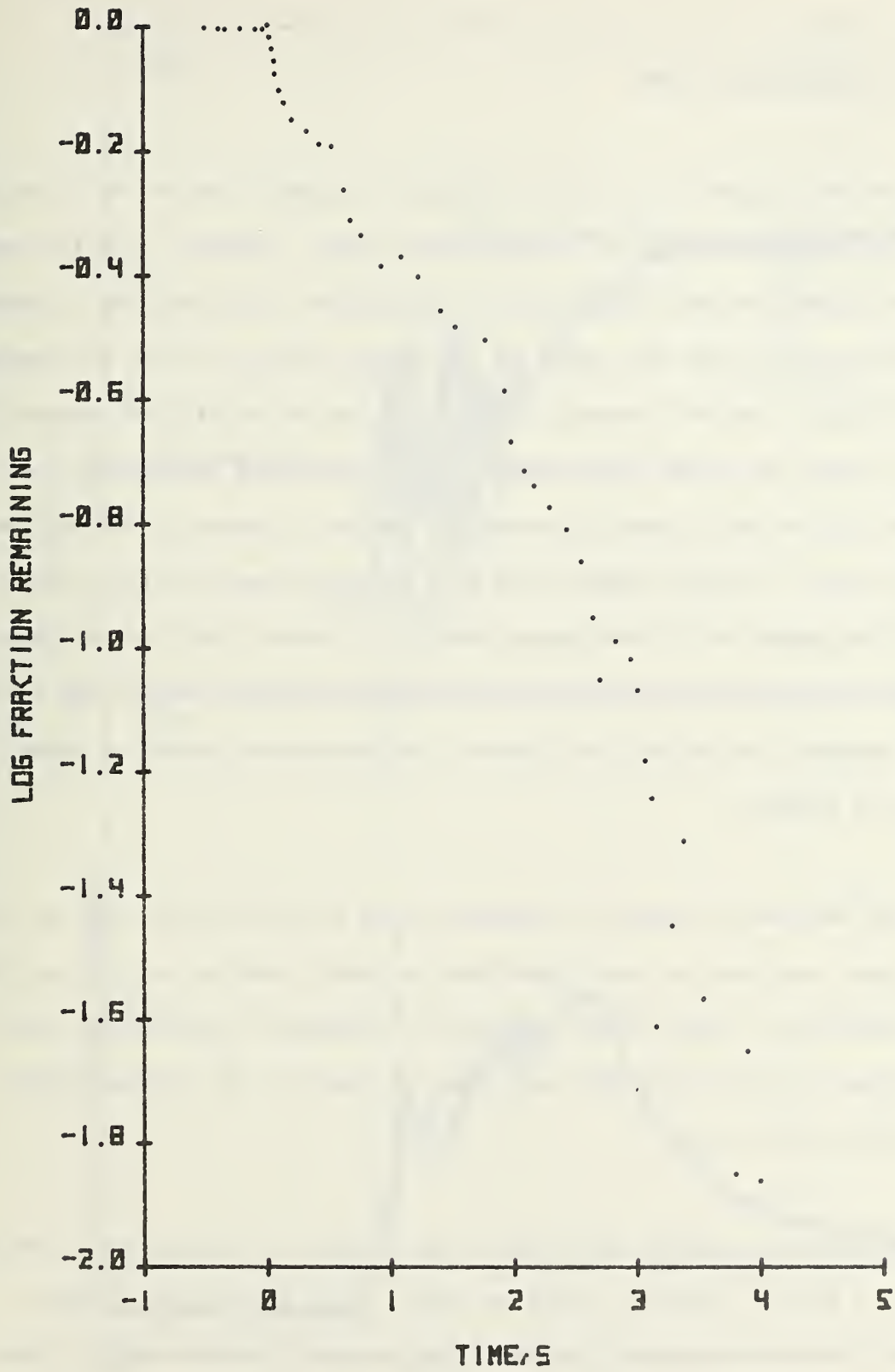


Figure 27. Log fraction remaining for 21-6-9 Stainless Steel.

### C. Nickel Alloy Inconel 600

This material proved to be quite difficult to ignite due to reflectivity of the alloy and the build up of a heavy oxide layer. However, once the sample ignited the combustion would usually go to completion. The material's combustion characteristics were very close to the ferrous alloys in that the combustion had irregular radiant intensity traces and ejected significant amounts of material. Figure 28b shows such a trace. The molten drop of material was usually very active and ejected considerable amounts of material during the combustion period. Usually there would be a quiescent period between the initial active phase and a final spray phase. It appears that the material must melt before ignition and sustained combustion can take place. The materials that comprise the molten drop appear to be completely mixed; no phase separation is evident.

The RSS was used to scan the combustion zone from 400 nm to 1100 nm. No emission lines were seen in this region and no vapor reaction regions were seen on film indicating no vapor-phase combustion. Combustion temperatures determined by using the RSS are in the same range as that for the ferrous alloys, 2500 to 2700 K (Table 3).

Weight-gain measurements were made in an attempt to determine the combustion rate. A typical result is shown in Figure 28a. As with the ferrous alloys the ejection of material presents some problems in obtaining an interpretable curve. However, since most of the material ejected was caught, it is believed that the curve in Figure 28a is a reasonably accurate representation

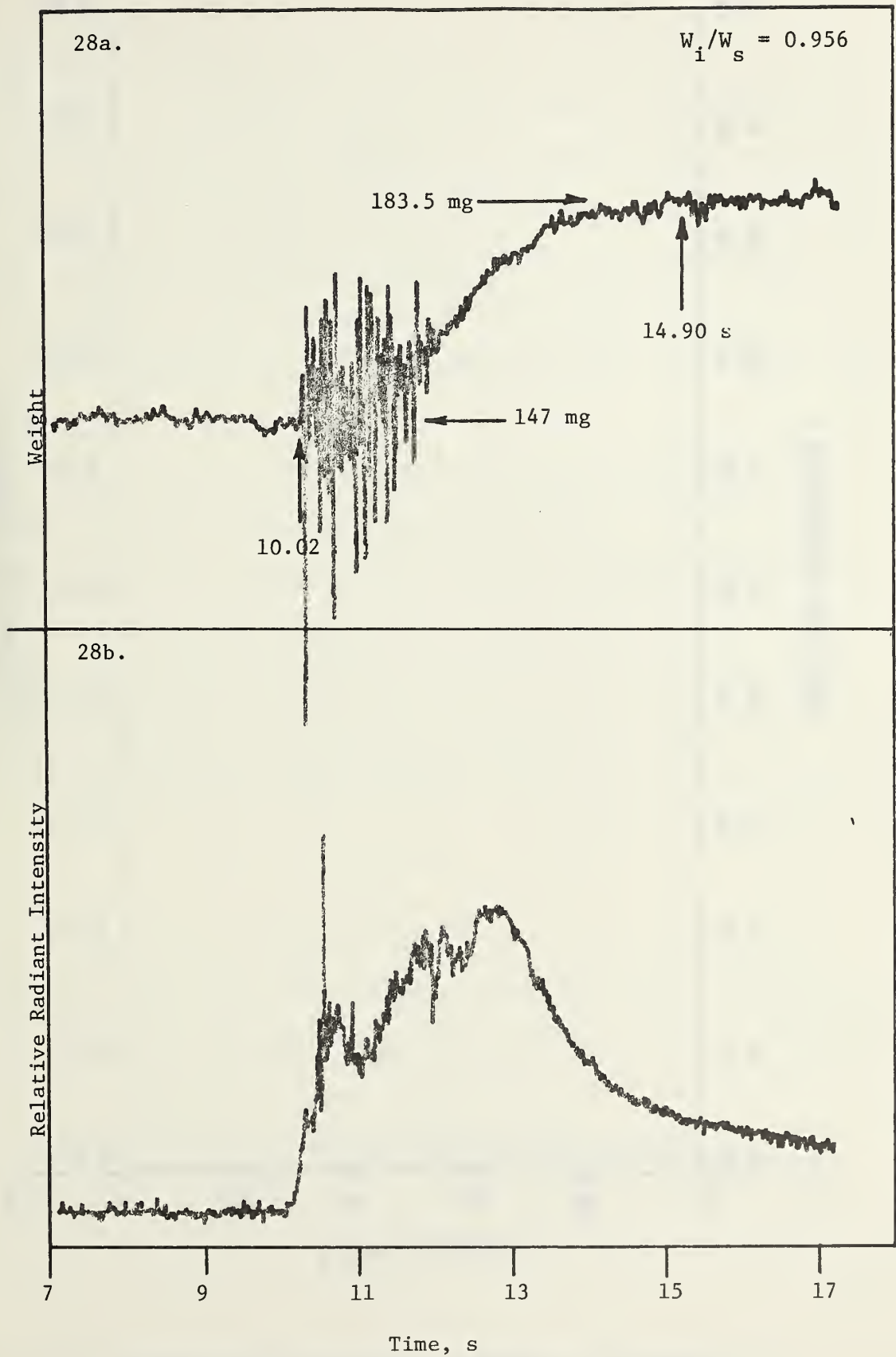


Figure 28. Inconel 600 combustion rate and radiant intensity.

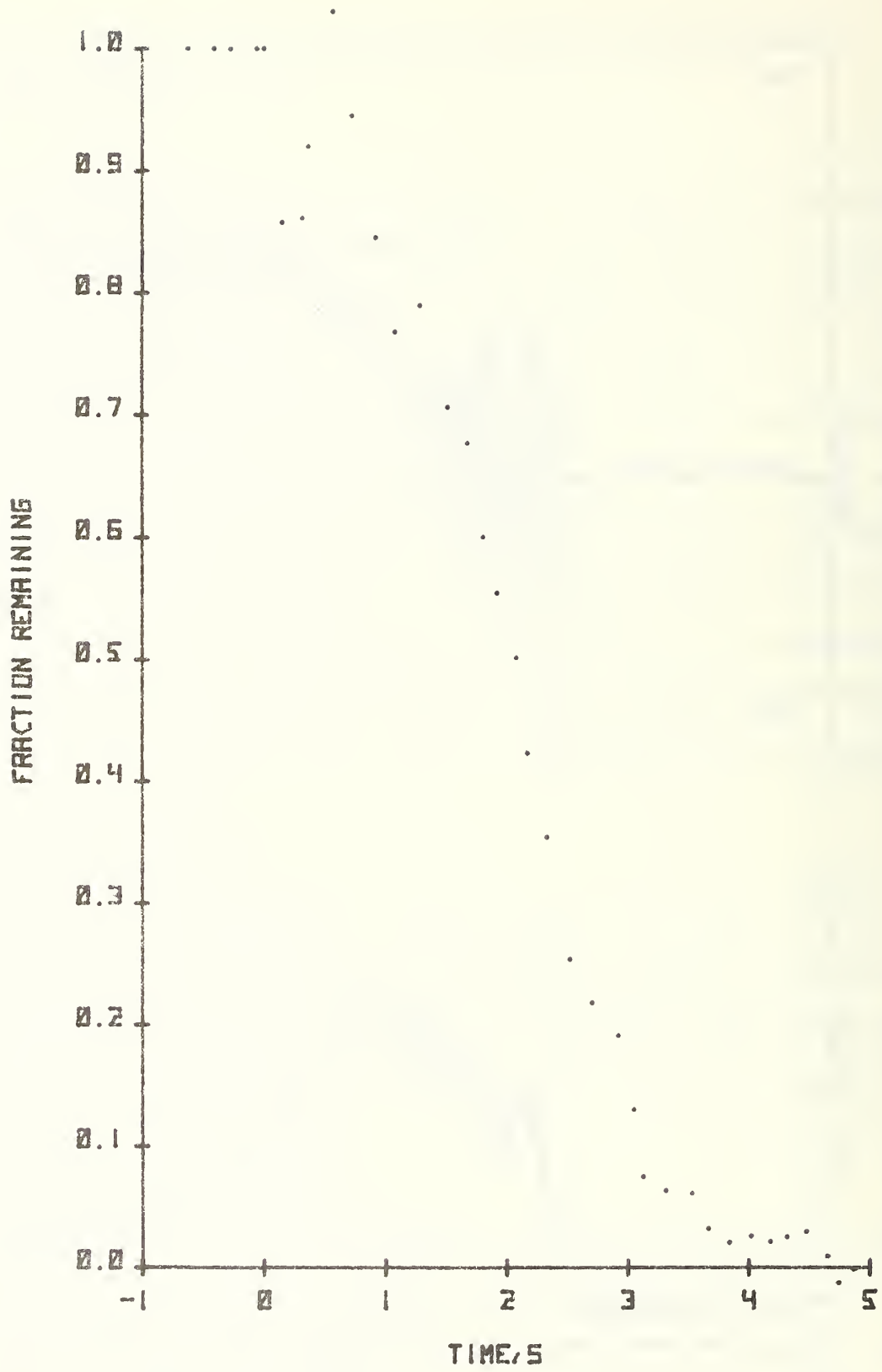


Figure 29. Fraction of Inconel 600 remaining during combustion.

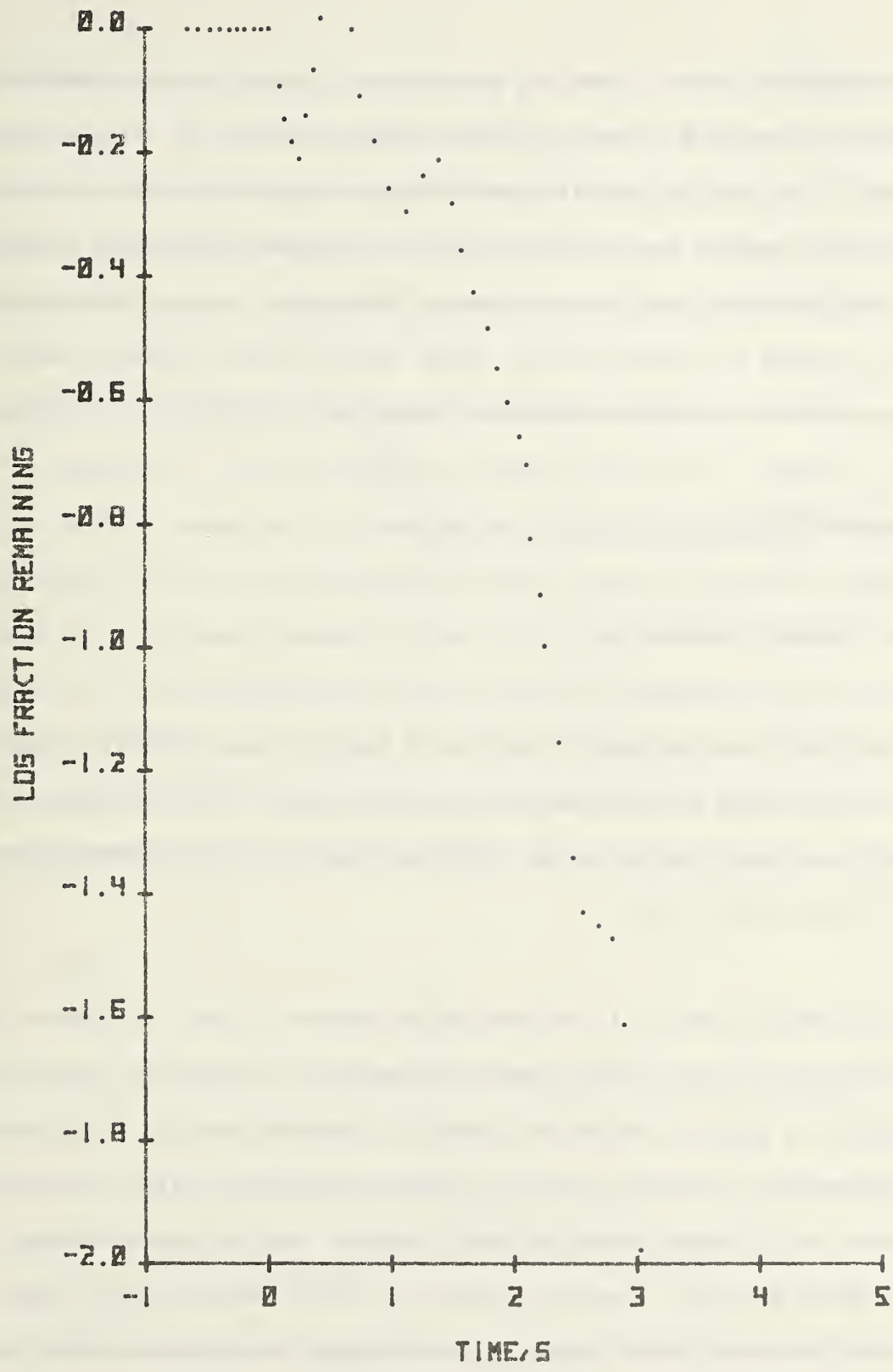


Figure 30. Log fraction remaining for Inconel 600.

of the combustion event. From the weight gain, curve fraction remaining and log fraction remaining curves were made, Figures 29 and 30. If the initial irregularity of the log fraction remaining curve is disregarded two approximately linear regions can be observed. These regions indicate an overall first-order reaction for the experimental arrangement. Like the stainless steels, a change in slope occurs at about the 50 percent consumed point, indicating a possible oxidation mechanism change.

#### D. Copper Alloys

##### 1. Beryllium-Copper

The beryllium-copper alloy was one of the two most difficult alloys to ignite. This alloy also had the most unusual radiant intensity trace. Figure 31b shows a typical example. The radiant intensity is approximately one eighth that of the ferrous alloys.

The induction phase of the combustion sequence is much like the other alloys studied. At some point after the sample has reached an incandescence temperature, a surface combustion front will advance from top to bottom and melt the sample. Combustion, with minimum drop activity, will proceed from this point with a small amount of spray ejected from the molten sample. Combustion is fast and of medium luminosity except for the initial flash. The oxides and unreacted alloy appear to mix completely; no phase separation is evident.

The combustion region was scanned from 400 nm to 1100 nm, using the RSS, for emission lines or bands from reacting vapor species. None were found nor was any vapor-combustion region evident on movie film indicating no vapor-phase combustion. Temperature measurements using the RSS gave maximum combustion temperatures between 2440 K and 2840 K (Table 3) for the molten sample.

Weight-gain measurements were made in order to determine the combustion rate. An example of a typical result is shown in Figure 31. Spikes, in the electrical signal, caused by the ejection of spray and droplets is a minor problem; however, the low stoichiometric factor (ratio of molecular weight of the oxides to the molecular weight of the alloy) does present a minor resolution problem. From the weight-gain curve, fraction remaining and log fraction remaining curves were made, Figures 32 and 33. It can be seen from the log fraction remaining curve that several approximately linear regions exist. This would indicate overall first-order reactions rates for the experimental setup.

## 2. Bronze

The bronze used in this study was easy to ignite. The combustion had a low luminous intensity with little to moderate amounts of spray and droplets produced. Drop activity during combustion was low. The oxides and unreacted alloy appear to be well mixed; no phase separation is evident.

The combustion zone was scanned from 400 nm to 1100 nm, using the RSS, for emission lines or bands from reacting vapor species. None was found nor was

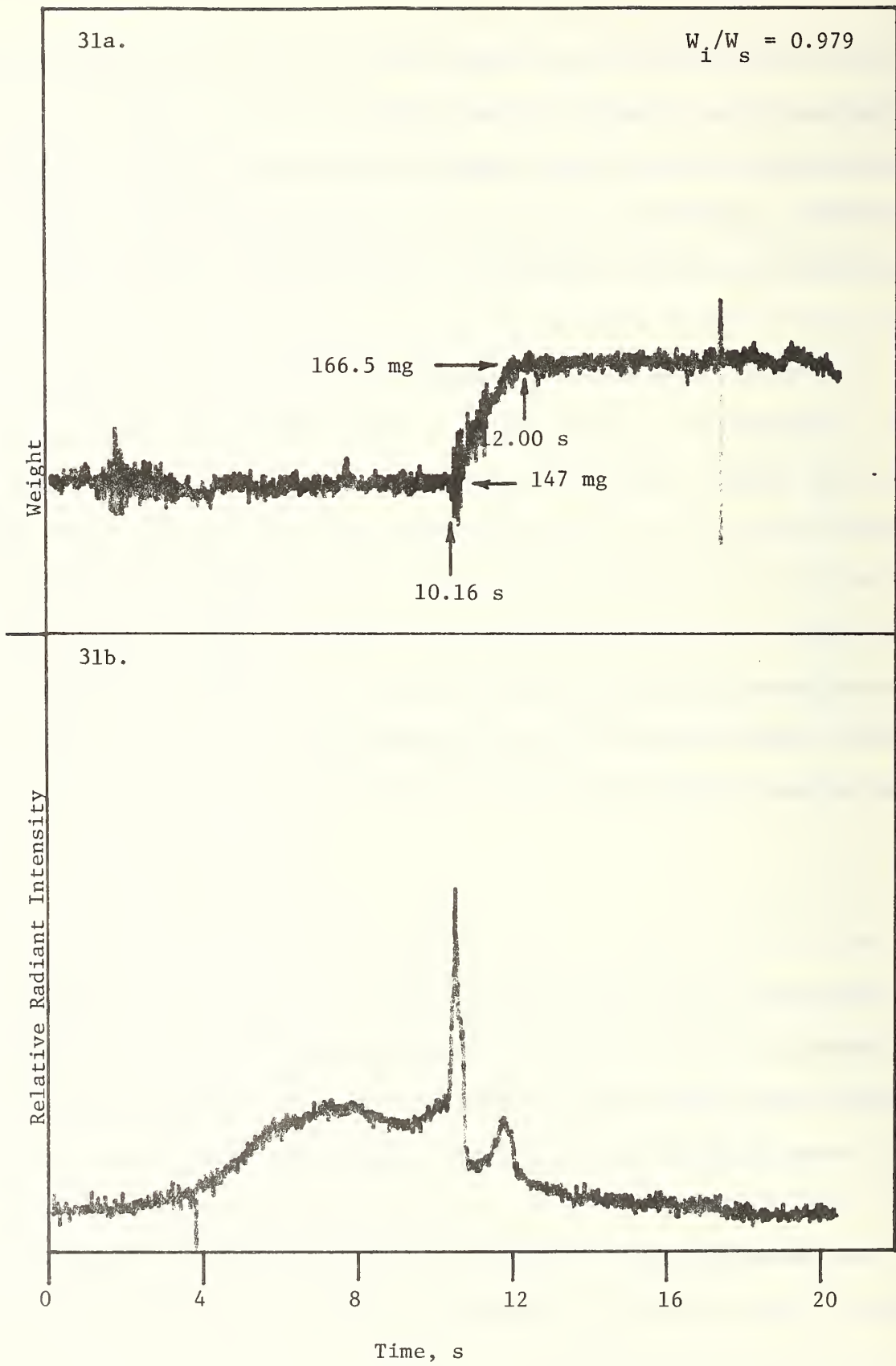


Figure 31. Beryllium-Copper combustion rate and radiant intensity.

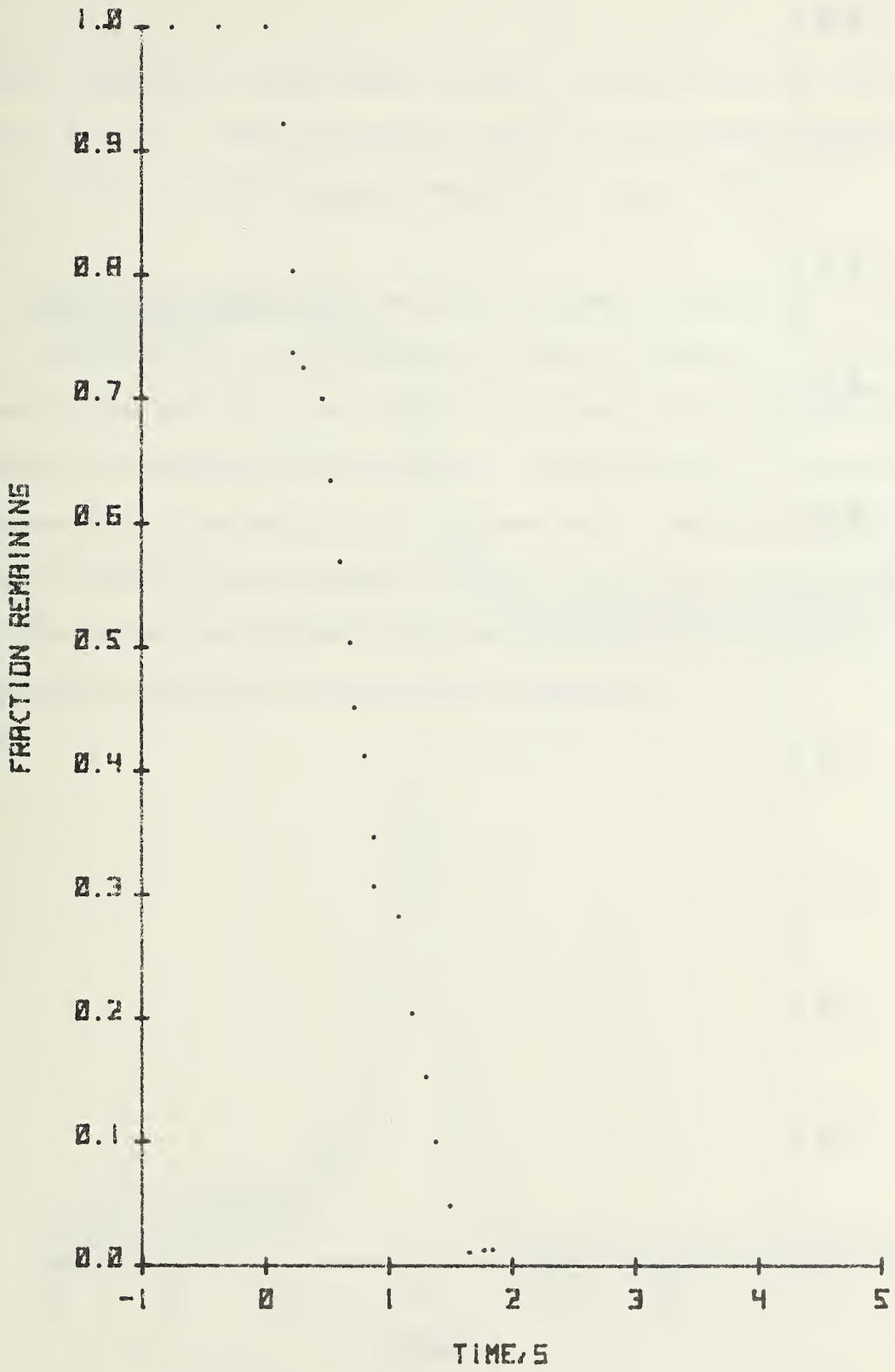


Figure 32. Fraction of Beryllium-Copper alloy remaining during combustion.

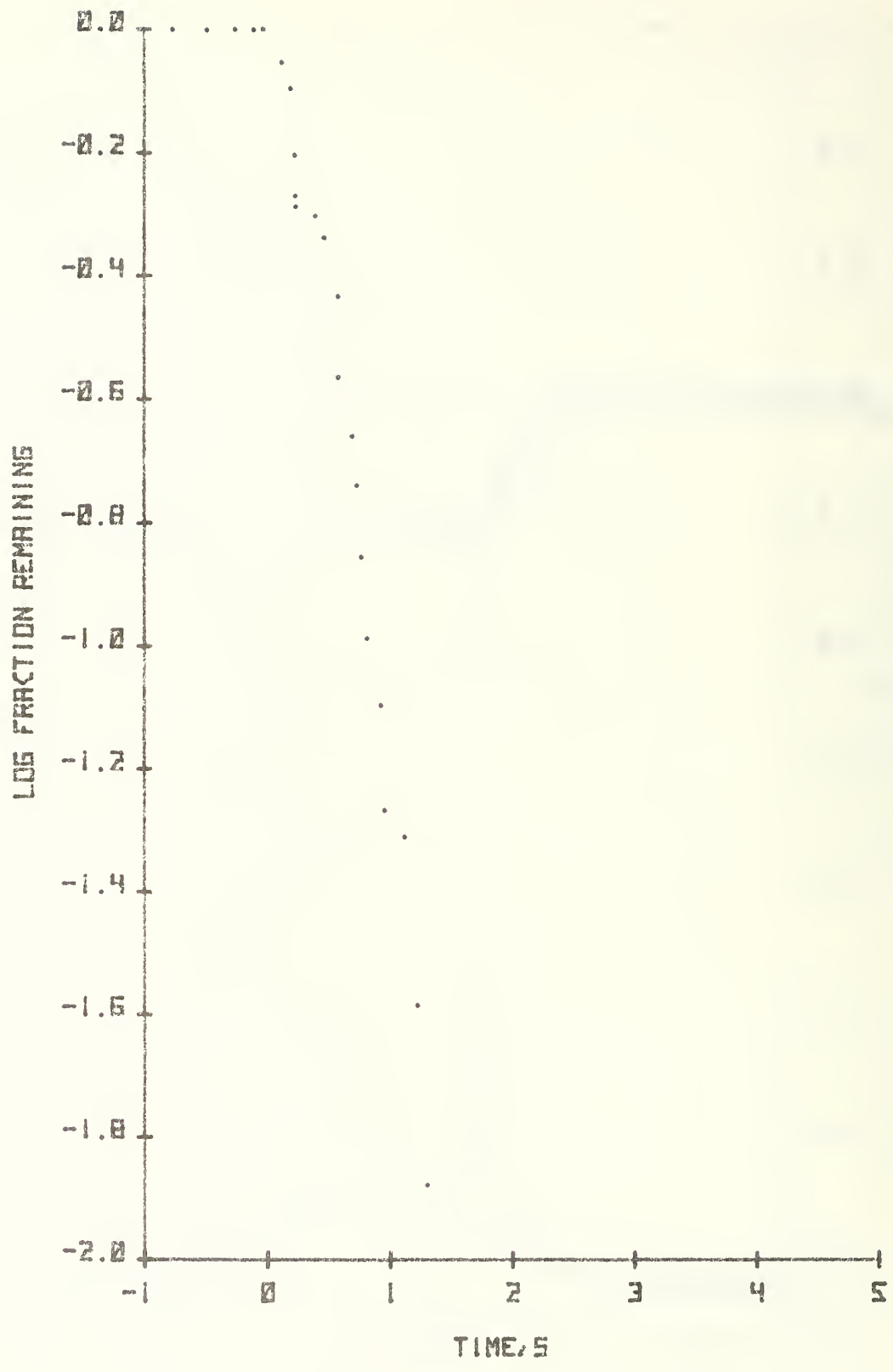


Figure 33. Log fraction remaining for Beryllium-Copper alloy.

any vapor-combustion region evident on movie film indicating no vapor combustion was present. Maximum combustion temperature measurements were also made using the RSS. The values ranged from 2075 K to 2250 K (Table 3).

Oxygen-uptake measurements were made in order to determine the combustion rate. An example of a typical results is shown in Figure 34. The material appears to have a high surface oxidation rate before the onset of combustion as determined from preignition observations. Essentially all of the material can be accounted for from the electronic balance data. Fraction remaining and log fraction remaining plots were made from the curve of Figure 34a (Figures 35 and 36). The log plot has predominately linear regions indicating first order combustion kinetics for the experimental arrangement.

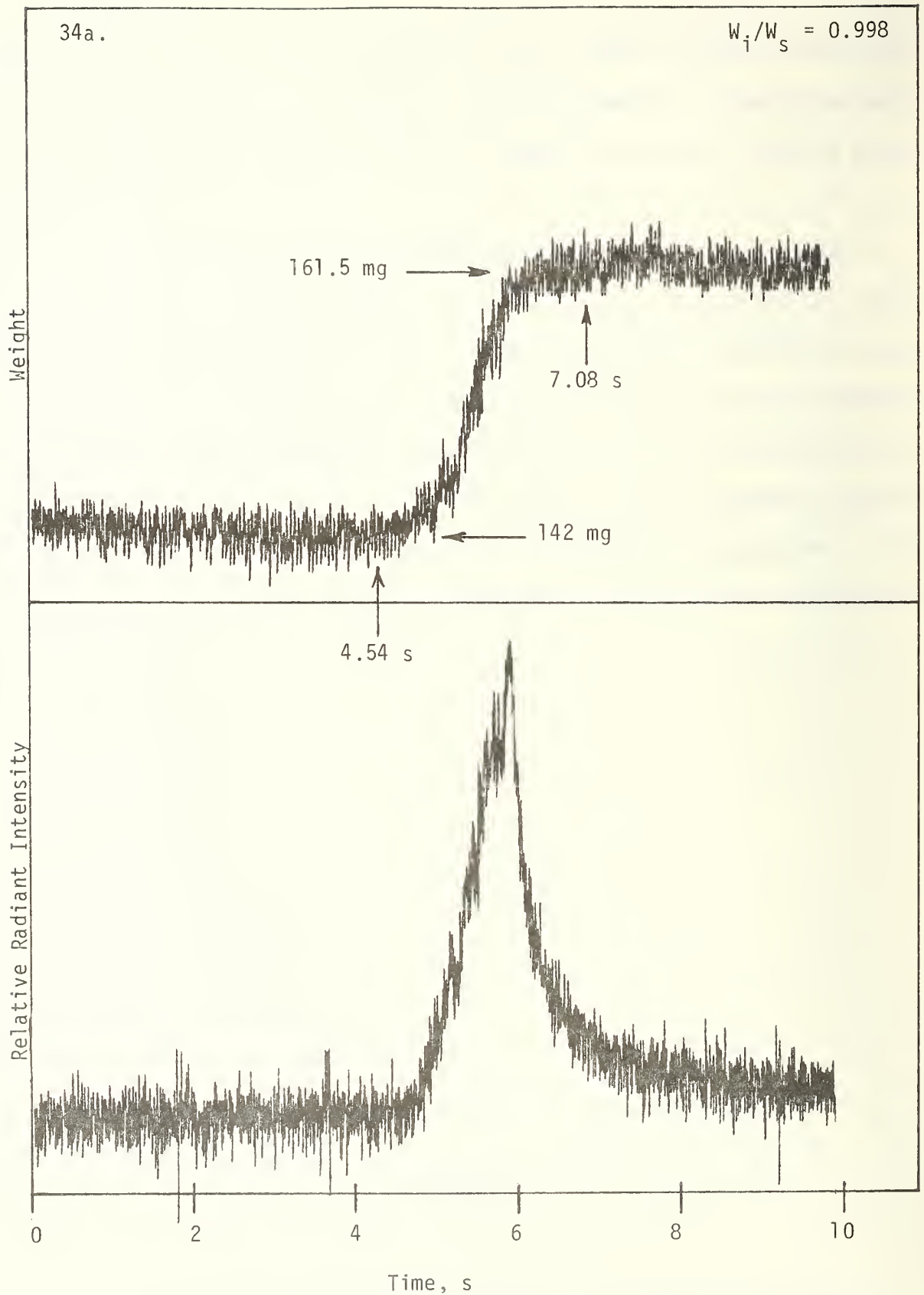


Figure 34. Bronze combustion rate and radiant intensity.

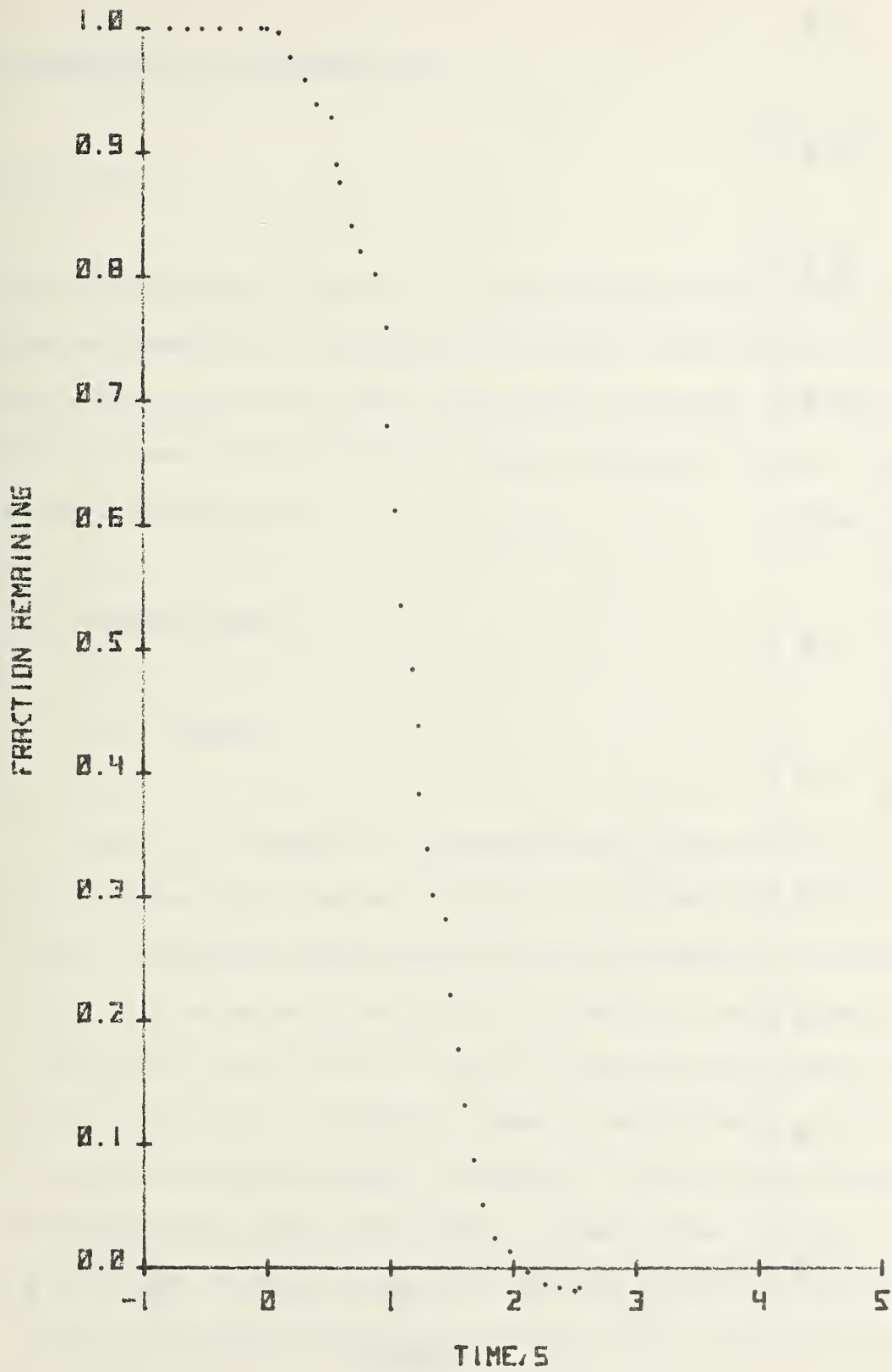


Figure 35. Fraction of Bronze alloy remaining during combustion.

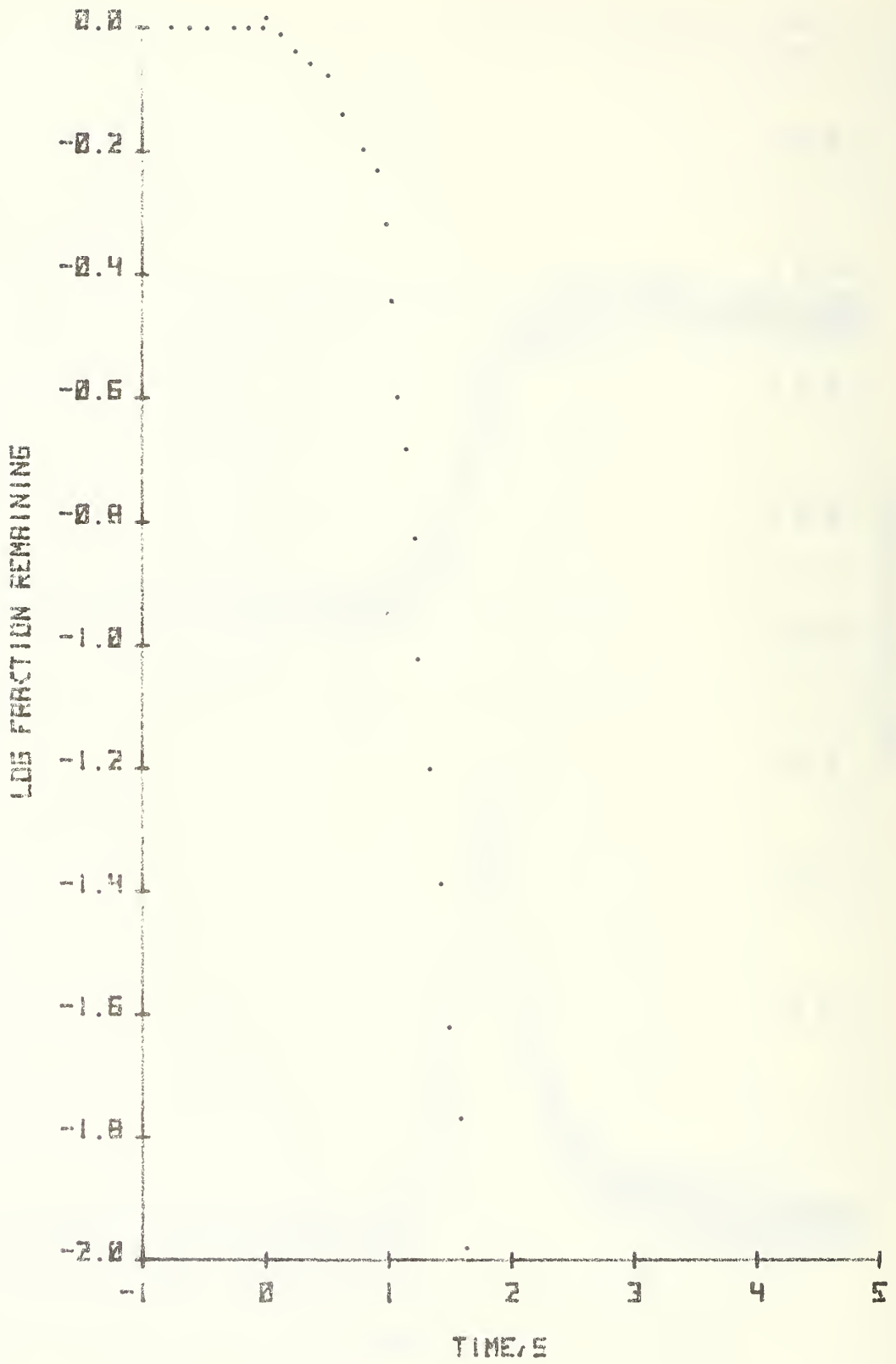


Figure 36. Log fraction remaining for Bronze alloy.

## IV. CONCLUSIONS AND RECOMMENDATIONS

### A. Conclusions

For this preliminary report, only tentative conclusions can be made on the ignition and combustion characteristics of metals in high-pressure oxygen. However, trends may be anticipated from chemical knowledge, past experiments, and the experiments reported herein. These anticipated trends are discussed below for each alloy group.

#### 1. Aluminum Alloys

##### a. Ignition

Ignition of aluminum and aluminum alloys normally does not occur at one atmosphere until the melting point of aluminum oxide is reached. This is due to the dense uniform nature of the oxide produced during heat-up, even on the molten metal surface, and to the fact that the vapor pressure of the molten alloy does not exceed one atmosphere until about the oxide melting point; thus a sufficient amount of metal vapor is not available for ignition until this point is reached. If other means are provided for removing the protective oxide layer, e.g. mechanical scraping, then ignition will occur at temperatures below the oxide melting point. For an undisturbed surface, the change in ignition point temperature may not vary

significantly with pressure; however, for a disturbed surface the ignition point may decrease significantly.

#### b. Combustion

For the experimental setup used in the experiments reported herein, the measured combustion temperatures are about 1000 K greater than the boiling point of the alloys, generally between 3300 to 3500 K (Table 3). This would indicate that the alloy is vaporizing then reacting with the oxygen. As system pressure is increased the boiling point of the alloy will increase, thus the molten alloy temperature, and the reaction rate will increase. Whether the reaction zone will collapse to the molten surface cannot be predicted with accuracy but may take place. In any event the reaction rates should increase considerably with the increase of oxygen pressure as will the combustion temperature.

## 2. Stainless Ferrous Alloys and Nickel Alloys

#### a. Ignition

The ignition temperature of these materials appear to be at or just below the materials' melting point. If the ignition takes place on a solid surface then we could expect a decreasing ignition temperature with pressure. This may also apply if ignition takes place at the alloy melting point. Whether mechanically disturbing the surface will effect the ignition point significantly cannot be predicted at this time.

## b. Combustion

The combustion temperatures of these alloys ranged from approximately 2400 K to 2700 K. If the combustion rate-determining process is oxygen diffusion controlled then an increase in pressure will increase the reaction rate and also the combustion temperature. Observing the intensity of the combustion process reported herein it can be anticipated that the combustion will be considerably more intense and active as the oxygen is increased, possibly to the point where the intensity is almost explosive in nature.

## 3. Copper Alloys

### a. Ignition

The ignition characteristics of the two copper alloys studied, a bronze and a beryllium-copper, were quite different. The bronze appeared to ignite at or just before melting, whereas the beryllium-copper appeared to ignite, after the alloy melted, at a fracture point on the oxide surface or at the oxide melting point. The high melting point of BeO is considered to be the reason for the difference in ignition characteristics between the two alloys.

For the bronze, if the ignition starts in the solid phase it can be expected that the ignition temperature would decrease for increasing

oxygen pressure. This may also be the case if the ignition takes place at a liquid phase.

For the beryllium-copper alloy no prediction on the pressure dependence of the ignition point can be made at this time.

#### b. Combustion

The combustion temperatures for the two alloys were not, on the average, vastly different - the bronze being 2165 K and the beryllium-copper being 2585 K - as might be expected from the completely different compositions. Since no vapor combustion was evident, it may be assumed that the combustion is diffusion controlled and that increased pressures would increase the combustion temperature and reaction rate. However, the predominant oxides,  $\text{CuO}$  and  $\text{Cu}_2\text{O}$ , are not refractory oxides and will decompose, thus limiting the combustion temperatures; beryllium-copper, due to the refractory nature of  $\text{BeO}$ , may not be limited in its combustion temperature until considerably higher temperatures are reached.

#### 4. Areas of Uncertainty

There are several areas which require a more detailed explanation than we can make at this time. These areas are:

1. The absence of emission spectra during the combustion of the ferrous, nickel and copper alloys.

2. The existence of several combustion rate constants (see figure 21 for example) each of which is apparently first-order or very nearly so.
3. The mechanism for the ejection of drops of material from the combusting parent mass.

Each of these areas probably requires a detailed knowledge of the chemical reaction mechanisms and the effect of the different chemical species upon one another in both a chemical and physical sense.

#### B. Recommendations

At present, a high pressure chamber has been designed in order to extend the studies into the high pressure region. Also the development of a high-speed two-color optical pyrometer has been undertaken in order to obtain accurate surface temperatures. With these two devices work can then begin on the determination of the high pressure ignition and combustion characteristics of the metals and alloys of interest. The present plans, and our recommendations, for the continuation of the present study call for the following action:

1. Procurement of the high pressure chamber and support equipment.
2. Procurement of optical equipment for the pyrometer development.

3. Concurrent with the above procurements, study, at one atmosphere, the combustion temperature pattern by optical Hilbert transform photography.
4. Upon receipt of high pressure chamber begin elevated pressure experiments. Obtain spectra, combustion rate, combustion temperature, and combustion behavior data.
5. Concurrent with the activity of items 4 and receipt of optical components, begin development of the two color pyrometer.

With successful implementation of these projects the program experimental objectives can be met.

In addition to the above recommendations we also suggest that effort be expended to design experiments and theoretical models that will explain the material ejection mechanisms, existence of several rate constants and the absence of spectra during the combustion of several of the materials.

#### V. ACKNOWLEDGMENTS

The authors would like to express their gratitude to Mr. John C. Moulder for his helpful discussion with and training of personnel performing this study; to Mr. James D. Breuel for his assistance in performing the experiments; to the George C. Marshall Space Flight Center, Mr. John G. Austin, Jr., technical representative, for funding this program.

## Appendix A: Temperature Measurements Using the Thermal Radiation Spectrum

Starting with the Planck radiation equation [1]

$$W_{\lambda T} = \frac{8\pi hc}{\lambda^5} \left( e^{\frac{hc}{\lambda kT}} - 1 \right)^{-1} \quad (1)$$

where  $\lambda$  = wavelength, m

$T$  = absolute temperature, Kelvin

$h$  = Planck's constant,  $6.626196 \times 10^{-34}$  J·s

$k$  = Boltzman's constant,  $1.380622 \times 10^{-23}$  J/K

$c$  = velocity of light in vacuum,  $2.997925 \times 10^8$  m/s

a wavelength range may be chosen such that the Planck equation may be approximated by Wien's approximation, that is

$$e^{\frac{hc}{\lambda kT}} = e^{\frac{hc}{\lambda kT}} - 1 \text{ for } \lambda \ll \frac{hc}{kT} . \quad (2)$$

Our wavelength range of 0.4 to 1.1 cm meets this requirement. The Planck equation thus reduces to

$$W_{\lambda, T} = \frac{c_1}{\lambda^5} e^{-c_2/\lambda T} \quad \text{where} \quad (3)$$

$$c_1 = 8\pi hc \text{ and } c_2 = \frac{hc}{k} .$$

[1] Light, Vol. 2; R. W. Ditchburn; Interscience Publishers.

Since the above equation applies only to a black body it must be modified to apply to a gray body. This is easily accomplished by multiplying by the spectral emissivity,  $\epsilon_\lambda$ . The Wien approximation then becomes

$$W(\lambda, T) = \epsilon(\lambda) c_1 \lambda^{-5} e^{-c_2/\lambda T} \quad (4)$$

This equation expressed in a logarithmic form yields

$$\ln W(\lambda, T) = \ln \epsilon(\lambda) + \ln c_1 - 5 \ln \lambda - c_2/\lambda T. \quad (5a)$$

which can also be written as

$$\ln W(\lambda, T) + 5 \ln \lambda = -\frac{c_2}{\lambda T} + \ln \epsilon(\lambda) + \ln c_1. \quad (5b)$$

If the assumption is made that the spectral emissivity is constant or reasonably so then the above equation has a linear dependence of  $(\ln W + 5 \ln \lambda)$  on  $1/\lambda$ . The temperature can then be determined from the slope of a plot of  $\ln W + 5 \ln \lambda$  vs.  $1/\lambda$ .

There are two major sources of nonlinearity. The first is the change in the value of emissivity with wavelength. This change is usually small over the visible and near infrared regions. Thus the change in the value of  $\ln \epsilon(\lambda)$  will be small and not contribute significantly to a nonlinearity in the curve. The second source of nonlinearity is in the determination of the values of radiant energy,  $W(\lambda, T)$ . If the value of  $W(\lambda, T)$  is in error by a constant multiplication factor (for example a calibration error) then this introduces a

constant error and shifts the curve along the vertical axis. This shift does not affect the value of the slope, thus an accurate temperature can be determined. If the value of  $W(\lambda, T)$  is in error by an additive error (for example, an error introduced in reading a photograph) then a small nonlinear perturbation to the curve can result. This type of error can usually be minimized by using least squares techniques in the data reduction.

Appendix B: Two-Color Pyrometer Theory  
by Key Nguyen and M. C. Branch

I. INTRODUCTION

Due to the large exothermic heat released and the transient nature of chemical reactions in metal combustion, any proposed method for measuring ignition and combustion temperatures faces two basic problems: high and rapidly changing temperatures and an oxidative environment. Such problems confine the measurement methods to radiation pyrometry. There are several advantages in employing radiation methods to temperature measurement. These are: (1) radiation methods confine disturbances of the system to the radiant energy leak emitted toward the detector; (2) theoretically there is no upper limit for measurable target temperature; (3) temperature measurements can be made on inaccessible targets; and (4) short response-time temperature measurements can be made. The last advantage is satisfied because the signal acquisition time is restricted only to the response time of the radiation detector, sampling electronics and recording methods. For the case of a photomultiplier detector, the response time is in the order of 10 ns.

One of the most commonly used methods of radiation temperature measurement is two-color pyrometry. In this method, the radiation emitted from the target is detected at two different wave lengths,  $\lambda_1$  and  $\lambda_2$ . From the ratio of radiation fluxes, the target temperature is then calculated (see eq. (B4)). Even though the method is quite versatile, there are still many disadvantages inherent to the method. For example, it must always be assured that the target has

to approach gray-body condition for the two wavelengths at which the measurements are made and that due to these restrictions, the measured surface temperature from a non-gray target obtained from two-color pyrometry tends to be higher than the true temperature. This is a characteristic feature of a two-color pyrometer. The reason is attributed to the fact that for most metals, the emissivity at shorter wavelengths has a larger numerical value than that at longer wavelengths (see eq. (B4)). Furthermore, for most real surfaces the emissivity is generally not only a function of wavelength but also of target temperature, direction and surface condition. This largely accounts for the fact that emissivity values listed in various reference books sometimes differ greatly. With this in mind, it is obvious that to reduce errors in temperature measurements resulting from the gray-body assumption, a method has to be devised to determine the spectral emissivity ratio  $\epsilon(\lambda_1, T)/\epsilon(\lambda_2, T)$ .

The temperature measurement system described herein is a modification of the method suggested by DeWitt and Kunz [1]. It is modified in order to have a short response time, in the order of 1 millisecond.

## II. THEORY OF THE MEASUREMENT METHOD

For a black body, the spectral radiance is related to the temperature and wavelength by the Planck radiation equation,

$$N(\lambda, b) = (c_1 \lambda^{-5} / \pi) / [\exp(c_2 / \lambda T) - 1] \quad (B1)$$

where:

$N(\lambda)$  = Radiation emitted at wavelength  $\lambda$ , per unit surface area, per unit wavelength interval, per unit solid angle.

$$c_1 = 3.74 \times 10^{-12} \text{ w}\cdot\text{m}^2$$

$$c_2 = 1.43 \text{ m}\cdot\text{k}$$

$T$  = Absolute temperature of radiating body, K

$\lambda$  = Wavelength of emitted radiation, m

For the case of real surface or non-black body, the spectral radiance is proportional to that of black body at the same temperature by

$$N(\lambda) = \epsilon(\lambda, T) N(\lambda, b) \quad (\text{B2})$$

where  $\epsilon(\lambda, T)$  is the spectral monochromatic emissivity.

For small values of  $\lambda T$  such that

$$e^{c_2/\lambda T} \gg 1$$

the Planck radiation equation can be approximated by the mathematically simpler form known as Wien's law

$$N(\lambda) = \epsilon(\lambda, T) c_1 \pi^{-1} \lambda^{-5} e^{-c_2/\lambda T} \quad (\text{B3})$$

For a body radiating at  $\lambda_1$ , and  $\lambda_2$  with corresponding spectral monochromatic emissivities  $\epsilon(\lambda_1, T)$  and  $\epsilon(\lambda_2, T)$ , it can be shown that the body temperature  $T$  is given by

$$\frac{1}{T} = \frac{1}{T_r} + \frac{\ln[\epsilon(\lambda_1, T)/\epsilon(\lambda_2, T)]}{C_2 \left[ \frac{1}{\lambda_1} - \frac{1}{\lambda_2} \right]} \quad (B4)$$

where  $T_r$ , the ratio temperature is given as

$$\frac{1}{T_r} = \left[ \frac{1}{\lambda_1 T_{s1}} - \frac{1}{\lambda_2 T_{s2}} \right] \cdot \left[ \frac{1}{\lambda_1} - \frac{1}{\lambda_2} \right]^{-1} \quad (B5)$$

in which  $T_{s1}$  and  $T_{s2}$  are the "apparent monochromatic temperatures" at wavelength  $\lambda_1$  and  $\lambda_2$ . In other words,  $T_{s1}$  and  $T_{s2}$  are the temperatures of a blackbody which at defined wavelengths  $\lambda_1$  and  $\lambda_2$  has the same radiation intensity as the body under consideration.

The above relations form the basis of "two-color" pyrometry. It is evident from eq. (B4) that for a graybody (where by definition emissivity is independent of wavelength), the spectral emissivity ratio  $\epsilon(\lambda_1, T)/\epsilon(\lambda_2, T)$  is unity and consequently, the second term of eq. (B4) is zero. In general, not all radiating bodies behave like graybodies, and hence the contribution of the spectral emissivity ratio to the measured temperatures has to be determined.

### III. DETERMINATION OF THE SPECTRAL EMISSIVITY RATIO

For a system in thermal equilibrium, Kirchhoff's law is applicable; that is,

$$\epsilon(\lambda, T) = \alpha(\lambda, T) \quad (\text{B6})$$

where  $\alpha(\lambda, T)$  is the absorptivity. Hence, it is possible to determine the spectral emissivity ratio  $\epsilon(\lambda_1, T)/\epsilon(\lambda_2, T)$  by direct measurement of the spectral absorptivity ratio,  $\alpha(\lambda_1, T)/\alpha(\lambda_2, T)$ . Of course the determination of the spectral emissivity ratio must be carried out under the same geometric conditions as that of the ratio temperature  $T_r$  as described by eq. (B4).

If the target is irradiated by a spectral line source, the energy  $E(\lambda)$  incident upon the target will cause a temperature rise  $\Delta T$ , proportional to the absorbed energy.

$$\Delta T = k_1 \alpha(\lambda, T) E(\lambda) \quad (\text{B7})$$

or, by Kirchhoff's law,

$$\Delta T = k_1 \epsilon(\lambda, T) E(\lambda) \quad (\text{B8})$$

If this process is performed at two different wavelengths,  $\lambda_1$  and  $\lambda_2$ , then the spectral monochromatic emissivity ratio given in terms of the spectral irradiances and their corresponding temperature rises is

$$\frac{\epsilon(\lambda_1, T)}{\epsilon(\lambda_2, T)} = \frac{E(\lambda_2)}{E(\lambda_1)} \cdot \frac{\Delta T_1}{\Delta T_2} \quad (\text{B9})$$

It should be emphasized here that to formulate the above relation, it is assumed that the proportionality constant  $k_1$  is the same for both conditions. This assumption is valid when the temperature rises,  $\Delta T_1$  and  $\Delta T_2$ , have the same order of magnitude and are much smaller than the target temperature.

Evidently to minimize the disturbances on the target, any temperature rise caused by laser irradiation has to be made as small as possible, and the lower limit of the temperature rise is restricted by the detectability of the radiation detector. With the extremely sensitive low-noise photomultipliers available it is expected that a temperature rise of approximately 0.05 K can be detected.

The temperature rises,  $\Delta T_1$  and  $\Delta T_2$ , can be observed at a different wavelength  $\lambda_0$  to minimize the effects of reflection from the target. The signal output  $S$  from the radiation detector will be proportional to the spectral radiance from the target

$$S = k_2 R(\lambda_0) \tau(\lambda_0) \epsilon(\lambda_0, T) N(\lambda_0, T) \quad (\text{B10})$$

where  $R(\lambda_o)$  is the absolute responsivity of the radiation detector,  $\tau(\lambda_o)$  the overall transmittance of the optical system, and  $k_2$  a proportionality constant which includes the effect of geometrical conditions.

By taking the differentials on both sides of the above relation, the change in signal output for a change in temperature of the target can be expressed as

$$\frac{\Delta S}{S} = \frac{C_2}{\lambda_o T^2} \cdot \Delta T \quad (B11)$$

Solving for  $\Delta T$  and then substituting into eq. (B9), this equation becomes

$$\frac{\varepsilon(\lambda_1, T)}{\varepsilon(\lambda_2, T)} = \frac{E(\lambda_2)}{E(\lambda_1)} \cdot \frac{\Delta S_1/S_1}{\Delta S_2/S_2} \cdot \frac{T_2^2}{T_1^2} \quad (B12)$$

At a high frequency of temperature measurement of the order of 1000 Hz, it is assumed that the temperature of the target essentially remains the same during the irradiation at two different wavelengths. Thus,  $T_1 = T_2$  and then it follows that  $S_1 = S_2$ , reducing the above relation to

$$\frac{\varepsilon(\lambda_1, T)}{\varepsilon(\lambda_2, T)} = \frac{E(\lambda_2)}{E(\lambda_1)} \cdot \frac{\Delta S_1}{\Delta S_2} \quad (B13)$$

The determination of the spectral emissivity ratio then essentially becomes the measurement of the incident laser energy upon the target at two different wavelengths, and the measurement of the corresponding change in photomultiplier signal output at a third wavelength.

#### IV. DESCRIPTION OF THE APPARATUS

A schematic diagram of the apparatus is shown in Fig. B1. The components of the apparatus can be separated basically into two different groups according to their functions: two-color temperature and spectral emissivity ratio measurements.

##### A. Two-Color Pyrometer

The heart of the system is the two-color pyrometer, which measures the "apparent monochromatic temperatures"  $T_{s1}$  and  $T_{s2}$  at two different wavelengths  $\lambda_1$  and  $\lambda_2$ .

The radiation flux from the target is focussed by an achromatic lens  $L_1$ , (300 mm focal length, 82 mm diameter) on a circular field stop inclined  $6^\circ$  to the optical axis with unity magnification to minimize spherical aberration. The emerging beam is then collimated by the lens  $L_2$  (100 mm focal length, 26.5 mm diameter), and the aperture is limited by the circular stop. The collimated beam with a beam diameter of 7 mm, then passes through a system of cube beam-splitters, rotating chopper disk and mirror.

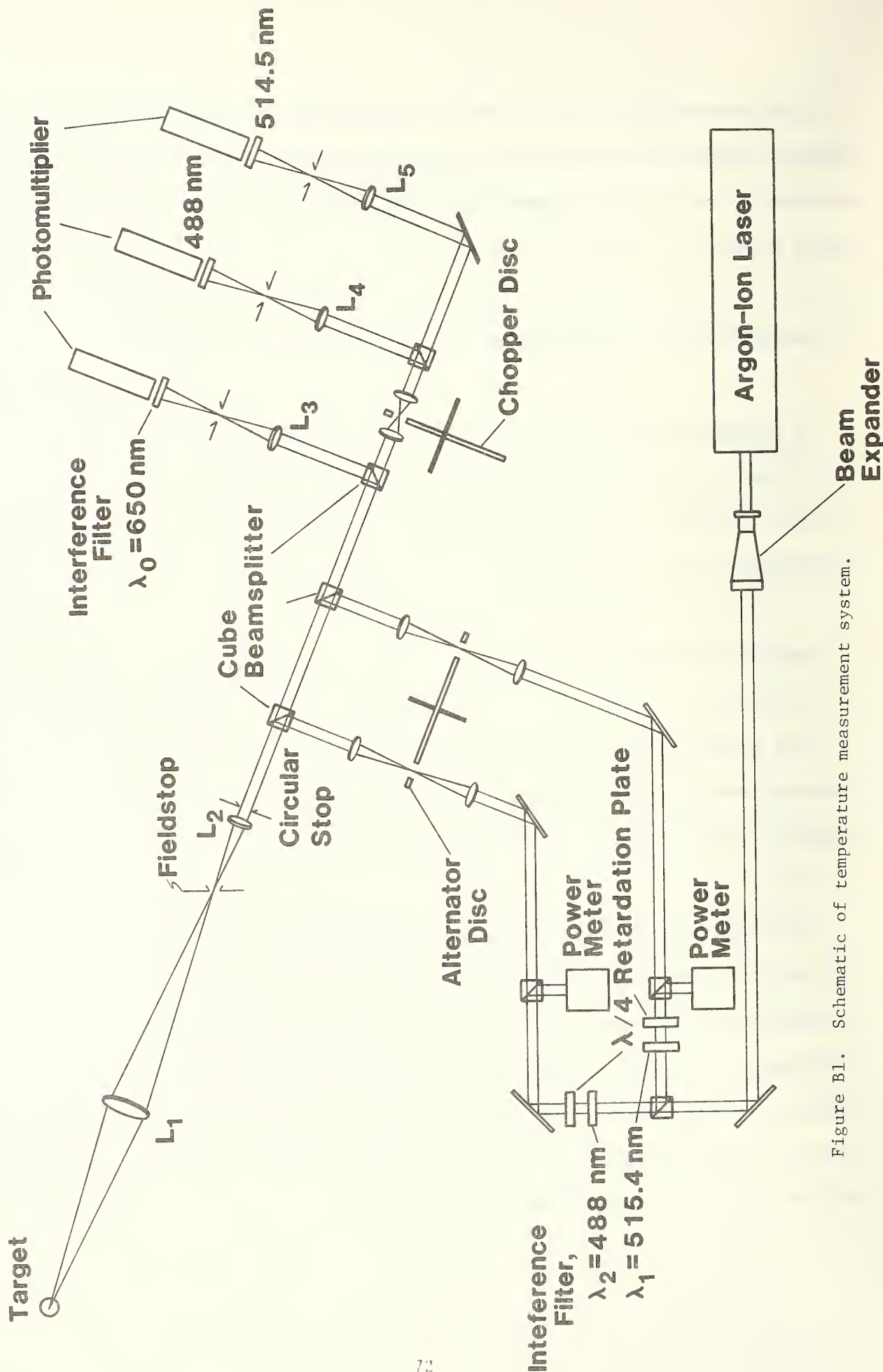


Figure B1. Schematic of temperature measurement system.

The chopper disk as shown in Fig. B2 has six large apertures each subtending  $30^\circ$  at the center of the disk. The chopper disk is rotated at 200 rps by a synchronous motor. With this arrangement, it is possible to chop the radiation flux from the target at a frequency of 1200 Hz. At this frequency, the chopping disk opens the radiation flux from the target for  $417 \mu\text{s}$ , then closes for  $417 \mu\text{s}$ .

The radiation fluxes reflected from the cube beamsplitter B4 are then focused by lenses  $L_4$  and  $L_5$ , which have the same characteristics and dimension as lens  $L_2$ , on the radiation detectors. These consist of two photomultipliers viewing the radiation fluxes through interference filters with wavelengths centered on 488 and 514.5 nm. The interference filters have a half height band width and peak transmittance of 3 nm and 50 percent, respectively. These two wavelengths are chosen such that to avoid any emission line or band spectra coming from the target. A preliminary study of spectra of burning Aluminum 1100, 2219, 6061 and Tensile-50, Inconel 600, Stainless Steel 304, 347, and 21-6-9, Beryllium-Copper and Bronze indicates that no emission line or band spectra exist at these two wavelengths. In addition, these two wavelengths are selected due to the inherent characteristics of argon-ion laser, which is to be discussed in the next section. The photomultipliers used to provide signal-detection are head-on types, with a peak response at 400 nm and a typical rise time of 15 ns.

## B. Spectral Emissivity Ratio Measuring Device

For irradiating the target, an argon-ion laser is used as a spectral line source. The laser is operated at all line operation, that is, the output beam

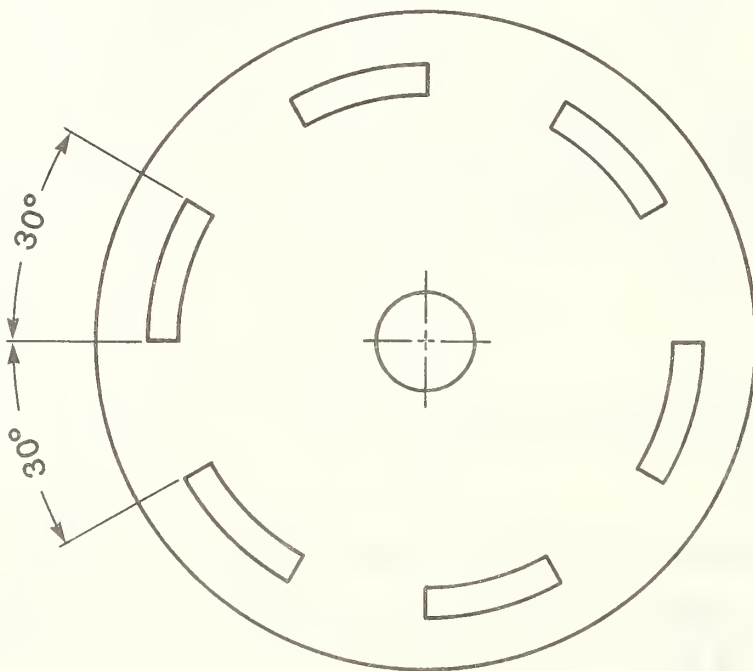


Figure B2. Chopper disk.

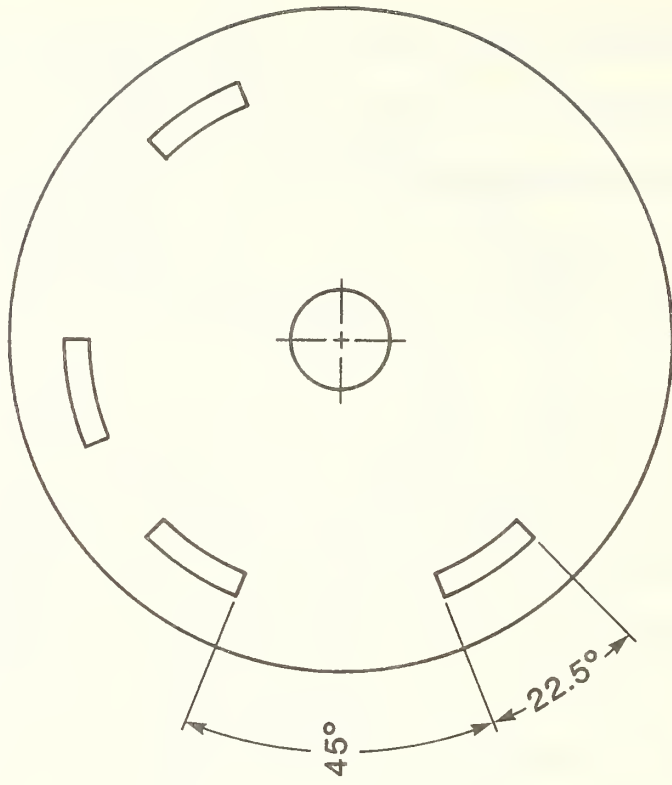


Figure B3. Alternator disk.

oscillates at eight different frequencies simultaneously. Furthermore, the laser is restricted to operation in TEM<sub>00</sub> Mode. This mode is selected to minimize diffraction loss, divergence, and, more importantly, to focus the beam to the smallest possible spot. The specifications and the spectral lines and their corresponding power outputs of the argon-ion laser are shown in Table B1 and B2, respectively.

As seen in Table B2, the power outputs in the various spectral lines of the argon-ion laser are quite different. At the spectral lines of 488.0 and 514.5 nm, the power outputs are largest and almost equal. It is always preferable to operate the laser at its maximum power output in order to achieve maximum output stability. The direct operating power outputs in the range of 25 mW to 145 mW can then be easily achieved by using a variable neutral density filter.

Due to the above considerations and the absence of emission line and band spectra coming from the target, the spectral lines of 488.0 nm and 514.5 nm are selected to irradiate the target in order to determine the spectral emissivity ratio.

To fill the aperture of the pyrometer, the output beam of the argon-ion laser is expanded by a beam expander by a factor of 5. The beam expander also provided spatial filtering for the laser beam. The expanded beam is then passed through a variable neutral density filter whose function is to control the beam power output.

To select 488.0 nm and 514.5 nm spectral lines, a system of cube beamsplitters and interference filters which have the same dimensions and characteristics

TABLE B1. SPECIFICATIONS OF ARGON ION LASER

Beam Diameter:	1.4 mm at $1/e^2$ Points
Beam Divergence:	0.8 mrad
Bore Configuration:	Segmented BeO with Integral Symmetrical Gas Return Channels
Resonator Construction:	Composition <sup>R</sup> (Composite Rod Ion Resonator Construction)
Excitation:	Current Regulated DC
Cavity Length:	1.15 m
Cavity Configuration:	Flat/Long Radius Spherical
Output Polarization:	1:100, Electric Vector Vertical
Noise:	Less than 0.3% rms - 10 Hz to 2 MHz (Measurement is made with a wide band photodiode driving a resistive load. The AC noise voltage is measured on an rms voltmeter with 10 Hz to 2 MHz bandwidth.)
Light Regulation:	(With optional Model 236.) Long term amplitude stability (1 second to 10 hours), better than 0.1% rms.
Power Measurement:	Integral, thermally stabilized ( $\pm 0.1^\circ\text{C}$ ), and wavelength corrected over spectral range from 450.0 to 700.0 nm. Accuracy is $\pm 5\%$ , full scale. 1-, 3-, 10-Watt Scales. Input jack for external power measurement.
Frequency Stability:	(With optional 423.) $\pm 75$ MHz.

TABLE B2. POWER OUTPUT OF THE ARGON ION LASER

WAVELENGTH	POWER, W
676.4 (Red)	
647.1 (Red)	
568.2 (Yellow)	
530.9 (Green)	
520.8 (Green)	
514.5 (Green)	1.400
501.7 (Green)	.200
496.5 (Green)	.300
488.0 (Blue)	1.300
482.5 (Blue)	
476.5 (Blue)	.500
476.2 (Blue)	
472.7 (Blue)	.100
468.0 (Blue)	
465.8 (Indigo)	.050
461.9 (Indigo)	
457.9 (Indigo)	.150
351.1/363.8 UV	
350.7/356.4 UV	
Total Power	4.000

as the ones used in the two-color pyrometer is employed. The expanded laser beam is directed onto a cube beamsplitter which passes 50 percent and reflects 50 percent of the beam. The split beams are then directed to interference filters, one to a filter centered on 488.0 nm and the other to a filter centered at 514.5 nm. Before the target is irradiated with these spectral lines, one condition has to be fulfilled. For example, the beam from the laser is usually plane polarized and it is necessary to depolarize the beam to correspond to the unpolarized conditions of the real radiating target. To achieve this a quarter wave retardation plate is inserted in the individual beam path with the retarder principal axis making an angle of  $+45^\circ$  with the electric field vector of the laser beam. The emergent beams are then circularly polarized. These two beams with wavelengths centered on 488.0 nm and 514.5 nm then travel parallel to each other, pass through the rotating alternator disk, and enter the two-color pyrometer optical path and are focussed in the same manner that the target is viewed.

The alternator disk, shown in Figure B3, is used to alternate the irradiation of two spectral lines upon the target. The increase in spectral irradiance as a result of laser flux incident upon the target is measured by a head-on photomultiplier at a wavelength centered on 650.0 nm.

#### V. THE VALIDITY OF THE THERMAL EQUILIBRIUM ASSUMPTION

As mentioned earlier, the determination of the spectral emissivity ratio  $\epsilon(\lambda_1, T)/\epsilon(\lambda_2, T)$  by direct measurement of the spectral absorptivity ratio is valid only if the target achieves a state of thermal equilibrium. Only in this

case is Kirchoff's law applicable. Although the heating effects due to laser irradiation of the target are, in general, not in thermal equilibrium with each other, no appreciable heating of the target occurs at least within the investigated power limits of 25 mW to 145 mW during the absorption of the incident laser irradiation, and Kirchoff's law is valid.

A state of local thermal equilibrium can be assumed if at some distance from the surface of the target the characteristic conduction time is less than the duration of the laser irradiation. The characteristic conduction time of the target  $\tau$ , with a characteristic dimension  $d = 100$  m is calculated from the following relation

$$\tau = \frac{d^2}{\alpha} \tag{B14}$$

where  $\alpha$  is the thermal diffusivity of the target. Typical values of characteristic conduction time of Al-1100, Ni and Inconel-600 are presented in Figure 4.

To satisfy the local thermal equilibrium assumption, the duration time of laser irradiation has to be adjusted according to the specimen. For example, in the case of Inconel-600, the duration time of laser irradiation is approximately 2.5 msec, whereas it is 0.2 msec for Al-1100.

[1] D. P. DeWitt and H. Kunz, "Theory and Technique for Surface Temperature Determinations by Measuring the Radiance Temperatures and the Absorptance Ratio for Two Wavelengths," Temperature - Its Measurement and Control in Science and Industry, Vol. 4, Part I, pp. 599-610 (1972).

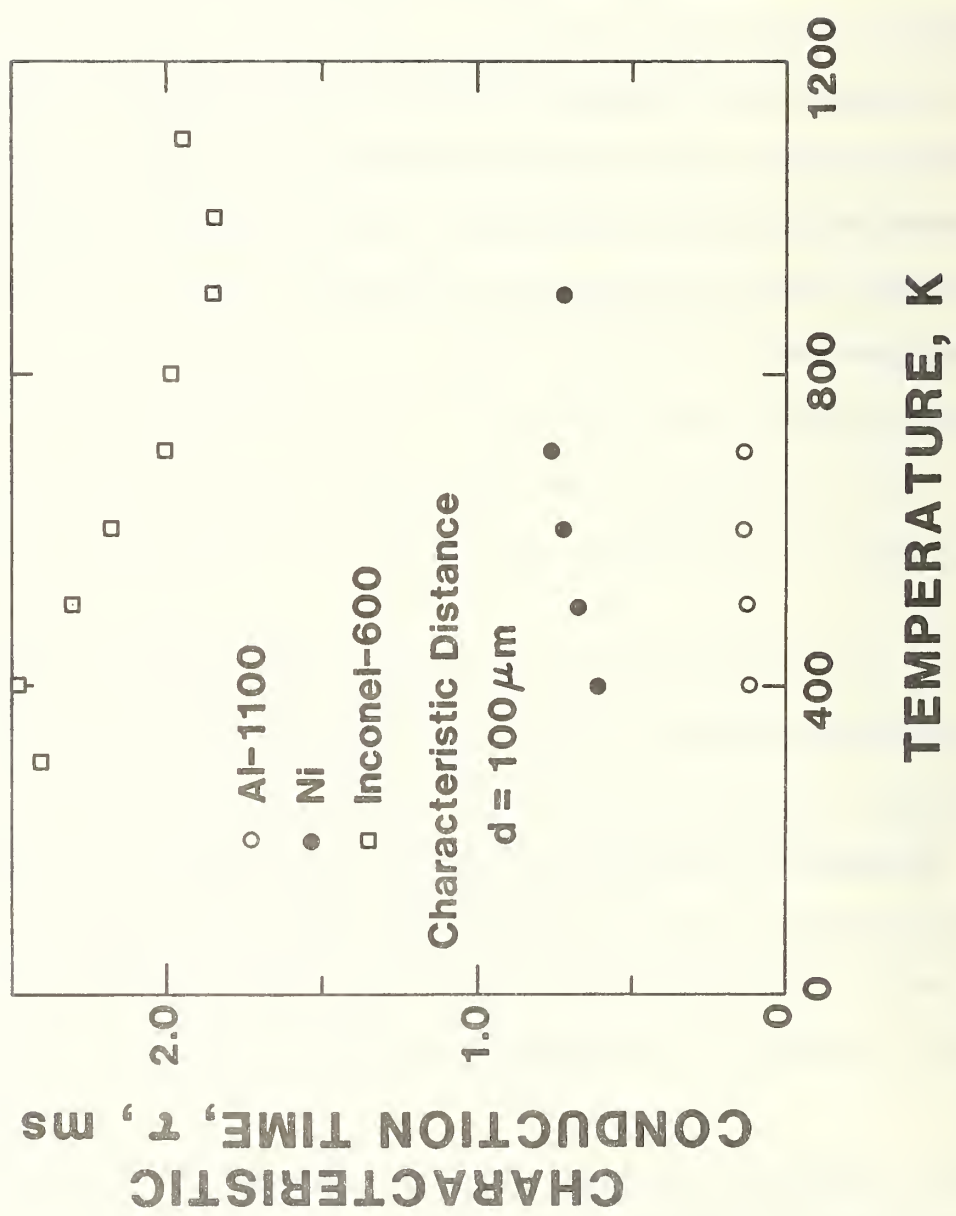


Figure B4. Characteristic conduction times of Al-1100, Ni and Inconel-600.

U.S. DEPT. OF COMM. <b>BIBLIOGRAPHIC DATA SHEET</b> <i>(See instructions)</i>	<b>1. PUBLICATION OR REPORT NO.</b> NBSIR 81-1647	<b>2. Performing Organ. Report No.</b>	<b>3. Publication Date</b> April 1981
<b>4. TITLE AND SUBTITLE</b> Laser-Initiated Combustion Studies of Selected Aluminum, Copper, Iron, and Nickel Alloys			
<b>5. AUTHOR(S)</b> J. W. Bransford and A. F. Clark			
<b>6. PERFORMING ORGANIZATION</b> <i>(If joint or other than NBS, see instructions)</i> NATIONAL BUREAU OF STANDARDS DEPARTMENT OF COMMERCE WASHINGTON, D.C. 20234		<b>7. Contract/Grant No.</b> Government Order H-43201B	<b>8. Type of Report &amp; Period Covered</b>
<b>9. SPONSORING ORGANIZATION NAME AND COMPLETE ADDRESS</b> <i>(Street, City, State, ZIP)</i> George C. Marshall Space Flight Center National Aeronautics and Space Administration Marshall Space Flight Center, AL 35812			
<b>10. SUPPLEMENTARY NOTES</b>  <input type="checkbox"/> Document describes a computer program; SF-185, FIPS Software Summary, is attached.			
<b>11. ABSTRACT</b> <i>(A 200-word or less factual summary of most significant information. If document includes a significant bibliography or literature survey, mention it here)</i>  <p>The results of combustion studies at atmospheric pressure on ten metal alloys are presented. The alloys studied were aluminum alloys 1100, 2219, 6061, and tensile-50; 304, 347 and 21-6-9 stainless steel; inconel 600; beryllium-copper and a bronze. It was found that once ignition was achieved all alloys would generally burn to completion. The overall combustion process appears to obey a first-order rate process. Preliminary conclusions are presented along with recommendations for future work.</p>			
<b>12. KEY WORDS</b> <i>(Six to twelve entries; alphabetical order; capitalize only proper names; and separate key words by semicolons)</i>  alloys; combustion; combustion rate; ignition; metals; oxygen atmosphere; <del>temperature measurement.</del>			
<b>13. AVAILABILITY</b> <input checked="" type="checkbox"/> Unlimited <input type="checkbox"/> For Official Distribution. Do Not Release to NTIS <input type="checkbox"/> Order From Superintendent of Documents, U.S. Government Printing Office, Washington, D.C. 20402. <input checked="" type="checkbox"/> Order From National Technical Information Service (NTIS), Springfield, VA. 22161		<b>14. NO. OF PRINTED PAGES</b> 89	<b>15. Price</b> \$9.50





